Mechatronics 64 (2019) 102296

Contents lists available at ScienceDirect

Mechatronics

journal homepage: www.elsevier.com/locate/mechatronics

Design of a fail-safe magnetorheological-based system for three-dimensional earthquake isolation of structures ☆

Sevki Cesmeci, Ph.D. [a,*], Faramarz Gordaninejad, Ph.D. [b], Keri L Ryan, Ph.D. [c], Walaa Eltahawy, Ph.D. [c]

[a] Department of Mechanical Engineering, Georgia Southern University, Statesboro, GA 30458, USA
[b] Advanced Materials and Devices, Inc, Sparks, NV 89502, USA
[c] Department of Civil and Environmental Engineering, University of Nevada, Reno, NV 89557, USA

ARTICLE INFO

Keywords:
Compressible damper
MR fluid
MR damper
Liquid compressibility
Fail-safe
Seismic isolation
Design
Optimization

ABSTRACT

This study presents a comprehensive design methodology for a magnetorheological-based damper device for a three-dimensional building isolation. The device acts as a suspension system itself by combining the liquid stiffness and controllable magnetorheological damping features in one unit. The bi-linear liquid stiffness feature enhances resistance to global rocking/overturning of the structural system by increasing the stiffness in the rebound mode compared to the compression mode. In the field, the system is combined with the conventional elastomeric bearings widely employed to mitigate the lateral seismic motions. During a seismic event, the system is subjected to dynamic vertical shaking and large lateral forces. The theoretical and simulation modeling to overcome this major challenge and achieve other system requirements are presented. In addition, a comprehensive optimization program is developed to achieve all design requirements. The modeling procedure is verified with experimental results. Also, the effectiveness of Displacement/Velocity-based control for a single degree-of-freedom system subjected to sinusoidal loading is evaluated.

1. Introduction

Current building codes require that buildings be designed for life safety when subjected to a design level earthquake, which is the strongest level of shaking expected to occur at the building site in a 475 year time frame, which corresponds to a 10% probability of exceedance in 50 years. A code conforming building may sustain significant structural damage and be uneconomical to repair after the earthquake. Furthermore, in several recent earthquakes, the majority of economic losses were reported to be due to the damage to nonstructural parts and contents of the building structures [1–2]. Seismic isolation technology has been developed to prevent damage to the structure and nonstructural components, and maintain the building operational after the earthquake [3,4]. With this technique, horizontally flexible devices (generally elastomeric bearings or sliding bearings) are placed beneath the building [5–6]. The flexibility of the isolators increases the fundamental period of the building and lowers the force demands.

Isolated buildings have generally performed well in past earthquakes, but they have not been rigorously tested in very large earthquakes [e.g. 7–9]. However, it has been shown in some of the recent shake table tests that the vertical component of shaking can cause damage to nonstructural components and contents even when the horizontal component of shaking is attenuated [10–12]. In [10], the damage to ceiling and piping systems was reported to be closely correlated to the intensity of vertical shaking and subsequent vertical vibration of the floor system. Significant vertical acceleration has not been reported in an isolated building during an earthquake; however, most reports do not mention vertical response. Vertical shaking is not rigorously considered in the design of an isolated building, and nonstructural component damage due to vertical shaking may compromise the ability of traditional seismic isolation systems to meet their design objectives [13].

Efforts were made to design efficient 3D building isolation systems primarily for the safe operation of nuclear power plants and facilities [14–15]. The designs proposed for this purpose included 3D isolation systems or vertical isolation systems that could be stacked together with existing horizontal seismic isolation devices [16–25]. Some other research focused on the vertical isolation of the lightweight hardware in buildings rather than the building isolation itself [26–28]. Yet, there is still not a generally acceptable solution for 3D isolation since some of

☆ This paper was recommended for publication by Associate Editor Charles Robert Koch, PhD.

* Corresponding author.
E-mail addresses: scesmeci@georgiasouthern.edu (S. Cesmeci), faramarz@unr.edu (F. Gordaninejad), klryan@unr.edu (K.L. Ryan), walaaeltahawy@nevada.unr.edu (W. Eltahawy).

https://doi.org/10.1016/j.mechatronics.2019.102296
Received 20 April 2019; Received in revised form 12 October 2019; Accepted 27 October 2019

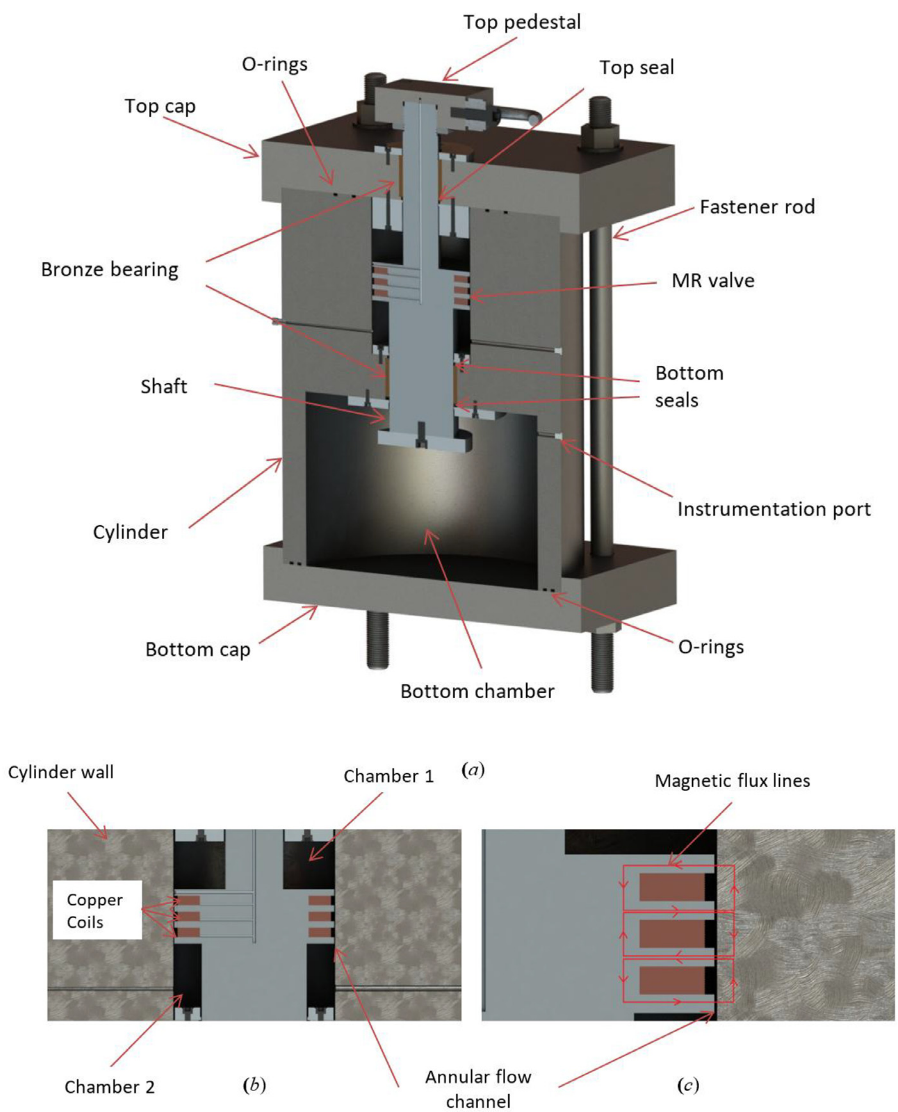

Fig. 1. (a) Cut-out view of the BLS-CMRD, (b) close up view of the MR valve, and (c) right half of the MR valve showing the magnetic flux lines and flow gap. (The space between the piston surface and copper windings were filled with a high strength epoxy, not shown here.).

these proposed solution are far from practicality and could be costly when implemented.

The authors propose a new fail-safe, compressible, controllable magnetorheological damper (called BLS-CMRD brevity for Bi-Linear Liquid Spring Controllable MagnetoRheological Damper) that would work as the vertical component of a 3D seismic isolation system. The device acts as a suspension system itself by combining the liquid stiffness and controllable MR damping features in a single unit. The bi-linear liquid stiffness feature enhances resistance to global rocking/overturning of the structural system by increasing the stiffness in the rebound mode compared to the compression mode. While the controllable MR damping could be beneficial when the device is subjected to excitations outside the design loading conditions. In the field, the device is combined with the conventional elastomeric bearings commonly used to mitigate the lateral seismic motions. During a seismic event, the device is subjected to both dynamic vertical shaking and large lateral forces. This is the first time an MR damping system has been proposed for such an application. MR dampers employ electromagnetic coils wound around a piston to activate the MR fluid to offer controllable damping. [29–30]. In the absence of magnetic field, the damper serves as a passive oil damper making the device fail-safe. A number of studies have focused on the design and characterization of compressible MR dampers [31–40], as reviewed in [41]. However, all these systems had relatively low force capacities, and they were all designed to resist loads in the axial direction only. The largest force capacity was reported to be 18 kN.

For this project, a one-quarter scale BLS-CMRD was designed, fabricated and experimentally characterized [41]. The scale model design forces were dynamic axial force = 245 kN, and constant shear force = 28 kN, respectively. A novel displacement/velocity-based (Disp/Vel-based) control strategy has been proposed for the device that adjusts the input current according to the instantaneous vector combination of feedback displacement and velocity of the damper [42]. The objective of this paper is to present a comprehensive approach for the design of BLS-CMRD for axial and shear loading requirements, and to evaluate the effectiveness of Disp/Vel-based control for a single degree-of-freedom system (BLS-CMRD with mass) subjected to sinusoidal loading.

2. Design of BLS-CMRD

Fig. 1a shows a 3D representation of the BLS-CMRD. The device is essentially comprised of a cylinder and a shaft like a typical shock absorber. The cylinder has two chambers sealed from each other. The shaft resides in the cylinder, and it has an extension to the lower chamber. The two caps seal the fluids in both chambers with the use of four external threaded rods. The upper chamber employs an MR fluid for both

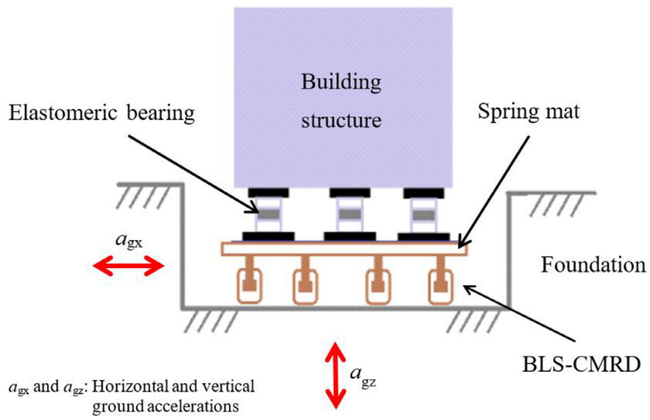

Fig. 2. Proposed installations of the BLS-CMRDs in the 3D isolation system.

controllable damping and liquid stiffness. The lower chamber uses pure silicone oil for the liquid spring only. The MR piston resides in the upper chamber. There is a narrow annular clearance between the piston and the cylinder wall where the fluid passes through between the two sides of the piston, i.e., Chamber 1 and 2 (Fig. 1b). The flow of the MR fluid through this narrow channel causes viscous energy dissipation and thus, a viscous damping. The piston has three separate copper coils. Once activated, an electromagnetic field is generated around the piston. The 2D representation of the field is shown in Fig. 1c. The small iron particles inside the MR fluid are forced to align in the direction of the magnetic flux lines forming a chain-like structure in the flow gap. To yield this chain-like structure, a pre-stress has to be applied on the fluid. This pre-stress (a.k.a yield stress), depends on the intensity of the applied magnetic field thereby providing a controllable damping. MR dampers are inherently fail-safe devices. In the case of a likely power outage to the device during a seismic activity or an electronic failure in the control system, the device can still operate in the passive-mode with some preset constant damping characteristics. This passive damping feature of the device is tailored based on the design loading conditions. The controllable damping feature is particularly beneficial when the device is exposed to excitations outside that design range.

The device also features two distinct liquid spring rates in rebound and compression modes. The shaft in the upper chamber has two different cross-sections on either side of the piston, i.e., higher cross-section below the piston. When pulled up, the additional shaft volume in the upper chamber compresses the MR fluid in this chamber causing a counter force by the fluid. This creates a spring effect, called liquid stiffness (or liquid spring). The shaft has an extension into the lower chamber. When pushed down, the shaft compresses the silicone oil in this chamber to provide a liquid spring. The different shaft geometries and chamber volumes as well as the different fluids in the chambers renders different spring rates in rebound and compression modes.

2.1. Design requirements

Fig. 2 shows the proposed installation of the BLS-CMRDs for practical application. These BLS-CMRDs are combined in series with the conventional horizontal isolators, such as elastomeric bearings, to support the building structure as depicted in Fig. 2. The building structure as a whole is excited by simultaneous horizontal and vertical earthquake acceleration (a_{gx} and a_{gz}, respectively) at the base; the earthquake acceleration in the out-of-plane horizontal direction is omitted from Fig. 2 for simplicity. According to the system dynamics, both sets of isolators will develop lateral and vertical forces to resist the earthquake accelerations. The lateral force demand is controlled by the design of the elastomeric bearings, but this lateral force will be transmitted to the BLS-CMRDs that must withstand it without yielding or fracture. Even when the shaft performs in the elastic region, the applied lateral force to the shaft may cause unbalanced stresses on the seals and may cause possible leakage. For this, whenever possible, the lateral displacement on the shaft has to be minimized.

Table 1
System requirements of the BLS-CMRD.

Static weight, W	92.8 kN
Frequency, f	4 Hz
Stroke, X	0.0254 m
Compression stiffness, k_c	6,000 N/mm
Rebound stiffness, k_r	24,000 N/mm
Viscous damping ratio, ζ	0.15 ~ 0.20
Shear force, F_S	27.84 kN
Allowable shear displacement, x	≤ 0.508 mm
Minimum structural factor of safety (FOS)	≥ 2
Dynamic range, D	> 2.5

The design strategy was developed based on a study discussing the structural dynamics of 3D earthquake isolation systems [43]. The axial and shear force demands to the device were determined from mapped spectral accelerations for a hypothetical Los Angeles, CA site, as discussed in [42]. As mentioned earlier, the device designed and tested for this project was a one-quarter length scale model, with force and displacement demands scaled accordingly relative to a theoretical full-scale prototype.

The device design requirements are summarized in Table 1. The target compression spring rate, k_c, calculated to be 6,000 kN/m, based on scale model design frequency $f = 4$ Hz ($f = 2$ Hz for a full scale prototype), and weight of 92.8 kN carried by the single device. The device was designed for two different liquid spring rates in rebound and compression modes. To aid resistance to overturning of the structural system, the rebound spring rate $k_r = 24{,}000$ kN/m, was selected to be 4 times the compression spring rate. The device was designed for a viscous damping ratio, ζ, in the range of 0.15 ∼ 0.20, to ensure that it can provide sufficient damping in the absence of magnetic field. The control-based application of magnetic field to increase the effective damping of the system was considered to be added protection against a larger than expected earthquake (see Section 5).

To ensure structural safety, the minimum structural factor of safety (FOS) was selected to be 2 against yielding for any component of the BLS-CMRD. The most critical component is the shaft since it is exposed to high shear stresses. In addition to yielding considerations, the shear displacement on the shaft was minimized for structural rigidity, as well as, to reduce the uneven stresses on the seals. The permissible lateral displacement of the BLS-CMRD was determined to be no more than 0.508 mm. The dynamic range, D, is given by [44]:

$$D = \frac{F_{\text{damper}}}{F_{\text{uncontrollable}}} = \frac{F_{\text{MR}} + F_{\text{viscous}} + F_{\text{friction}}}{F_{\text{viscous}} + F_{\text{friction}}} = 1 + \frac{F_{\text{MR}}}{F_{\text{viscous}} + F_{\text{friction}}} \quad (1)$$

where F_{MR} is the controllable force, F_{viscous} is the passive viscous damping force, and F_{friction} is the seal friction force. D, which represents the ratio of the total damper force to the uncontrollable damping forces, is a measure of the performance of an MR damper. The dynamic range, D, for BLS-CMRD was targeted to be greater than 2.5 at the design frequency and stroke.

The device was designed by analytical modeling and simulation according to the methodology illustrated in Fig. 3. Analytical equations for design forces were used to select basic dimensions of the device. The sizes of the top and lower chambers, and the shaft were determined using equations for the bi-directional liquid spring force, F_{spring} according to the rebound and compression stiffnesses given in Table 1. Then, the seal friction force, F_{friction} was estimated. Next, parameters were selected to achieve the fail-safe viscous damping force, F_{viscous} according to the damping ratio listed in Table 1. Lastly, parameters were selected to achieve the controllable MR damping force, F_{MR} in accordance with

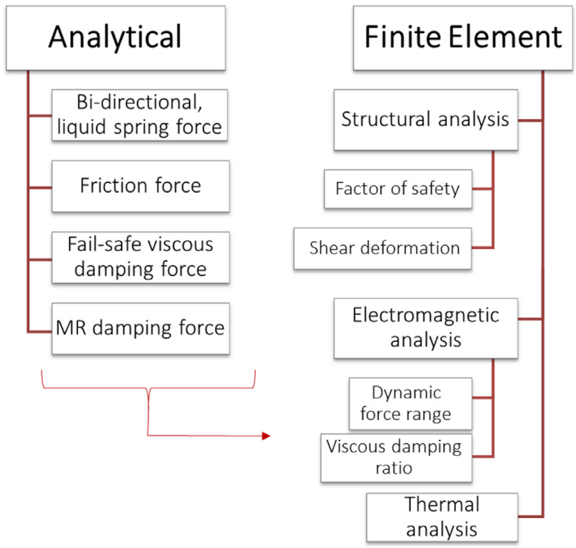

Fig. 3. Design methodology for the BLS-CMRD.

the dynamic range, D given in Table 1. The viscous and MR damping forces determined the dimensions of the MR valve (Fig. 1*b*).

The design process was enhanced by simulation to address the following additional considerations. The MR damping force, which involves the calculation of the magnetic flux density developed in the flow gap, is best predicted via computer simulations, as available analytical equations may not provide enough accuracy. In addition, the shear displacement and forces pertaining to structural FOS in Table 1 are evaluated through a structural analysis aided by software packages. The temperature of the MR fluid in the upper chamber increases due to viscous energy dissipation in the fluid and Ohmic losses in the coil circuit. This affects the performance of the device. A computer aided thermal analysis is used to evaluate the temperature field inside the device as well as the cooling time required for the consistency of the results during testing.

To achieve all these design requirements, a comprehensive optimization program was developed in Ansys platform. The key geometric design parameters used in analytical and finite element modeling are shown in Fig. 4. $C_{b,\text{ step}}$ is the radial distance between the surface of the bottom shaft and inner wall of the lower chamber, L_3 is the length of the lower chamber, R_{sb} is the radius of the bottom shaft, R_{st} is the radius of the top shaft, R_p is the radius of the piston, h is the annular clearance in the MR valve, L_2 is the length of the Chamber 2, L_1 is the length of the Chamber 1, L_{piston} is the length of the piston, L_a is the length of active pole (metal parts of the piston in the flow channel), L_p is the length of passive pole (length of the coil). The details of each step of the analysis are described in the following sections.

2.2. Analytical modeling

The total force of the BLS-CMRD can be expressed as the superposition of the bi-linear liquid spring force, F_{spring}, friction force, F_{friction}, fail-safe viscous damping force, F_{viscous}, and controllable MR damping force, F_{MR}. The spring force for liquids is described as the multiplication of a spring rate and displacement of the spring shaft into the spring chamber. The spring rate is a function of material and geometric parameters and is given as [45]:

$$k_i = \beta \frac{A_{s,i}^2}{V_i} \tag{2}$$

where β is the bulk modulus of the fluid, $A_{s,\,i}$ and V_i are the shaft cross-section and the fluid volume in chambers, respectively. If there is a pre-pressurization in chambers, then the total spring force becomes the summation of the spring force and hydrostatic pressure force on the shaft,

$$F_{\text{spring}} = k_i x_{s,i} + P_i A_{s,i} \tag{3}$$

where P_i is the initial pressure in specific chamber, and $x_{s,\,i}$ is the displacement of the shaft.

The friction force in the BLS-CMRD results from the mechanical friction between the seals and shaft. In this design, the top and lower chambers were sealed from each other with two seals on either end of the bottom bearing, whereas the upper chamber was sealed from the outer environment via one seal on the bottom side of the top bearing. The seal lips must be in contact with the shaft surface at all times during operation. The seals were designed so that when the pressure of the liquid in a specific chamber increases, the seal lip presses on the shaft more firmly. This results in an additional friction force. This behavior of the seals can be characterized by separating the total friction force into two components: quasi-static and dynamic frictions, as follows:

$$F_{\text{friction}} = F_f + F_{f,d} \tag{4}$$

The constant quasi-static friction force, F_f, can be determined experimentally by testing the device under quasi-static loading conditions, i.e., at very low speeds avoiding any inertial effects. The dynamic seal friction force, $F_{f,\,d}$, is given, as follows:

$$F_{f,d} = \frac{1}{2} A_{\text{sl}} \Delta P \tag{5}$$

where A_{sl} is the area of the seal in contact with the shaft surface, ΔP is the pressure difference across the seal. In the absence of magnetic field, the system works in the fail-safe mode as a passive damper. When the shaft pushes down, the fluid flows from Chamber 2 to Chamber 1 through MR valve thereby generating a viscous dissipation (Fig. 1*a, b*). When h/D_p is small enough, the flow through two hollow cylinders can be accurately approximated as a flow through two large parallel plates. This assumption is validated by Table 2. The force generated due to the viscous flow through two large parallel plates is given by [44]:

$$F_{\text{viscous}} = \left(1 + \frac{whV_p}{2Q}\right) \frac{12\mu Q L_{\text{piston}} A_p}{wh^3} \tag{6}$$

where Q is the flow rate through the MR valve, h is MR valve thickness, L_{piston} is the piston length, w is the mean circumference of the MR valve, V_p is the velocity, μ is the dynamic viscosity, and A_p is the effective area. Because it is proportional to velocity, the viscous force is rate and frequency dependent. Eq. (6) assumes steady flow and constant flow properties. Under magnetic field, the MR fluids behave as non-Newtonian fluids, and this behavior of the MR fluids can be effectively represented by the Bingham plastic model as follows [46]:

$$\tau = \tau_y + \mu\dot{\gamma}; \qquad \tau > \tau_y \tag{7}$$

where τ is the shear stress, τ_y is the yield stress, μ is the plastic viscosity, and $\dot{\gamma}$ is the shear strain rate. τ_y is a function of the magnetic field and can be controlled with the intensity of the applied magnetic field. The controllable MR force is given by [44]:

$$F_{\text{MR}} = \left(2.07 + \frac{12Q\mu}{12Q\mu + 0.4wh^2\tau_y(B)}\right) \frac{\tau_y(B) L A_p}{h} \operatorname{sgn}(V_p) \tag{8}$$

where L is the active pole length and $\tau_y(B)$ is the field-dependent shear stress.

The total device force can be calculated by superimposing the spring, friction, passive damping, and controllable damping forces:

$$F_{\text{device}} = F_{\text{spring}} + F_{\text{friction}} + F_{\text{viscous}} + F_{\text{MR}} \tag{9}$$

and is plotted in Fig. 5 for a sinusoidal excitation of 0.0254 m at 4 Hz, and 1 A applied current. The different A_p's in Eqs. (6) and (8) yield different force levels for the rebound and compression modes resulting in an asymmetric force around x-coordinate.

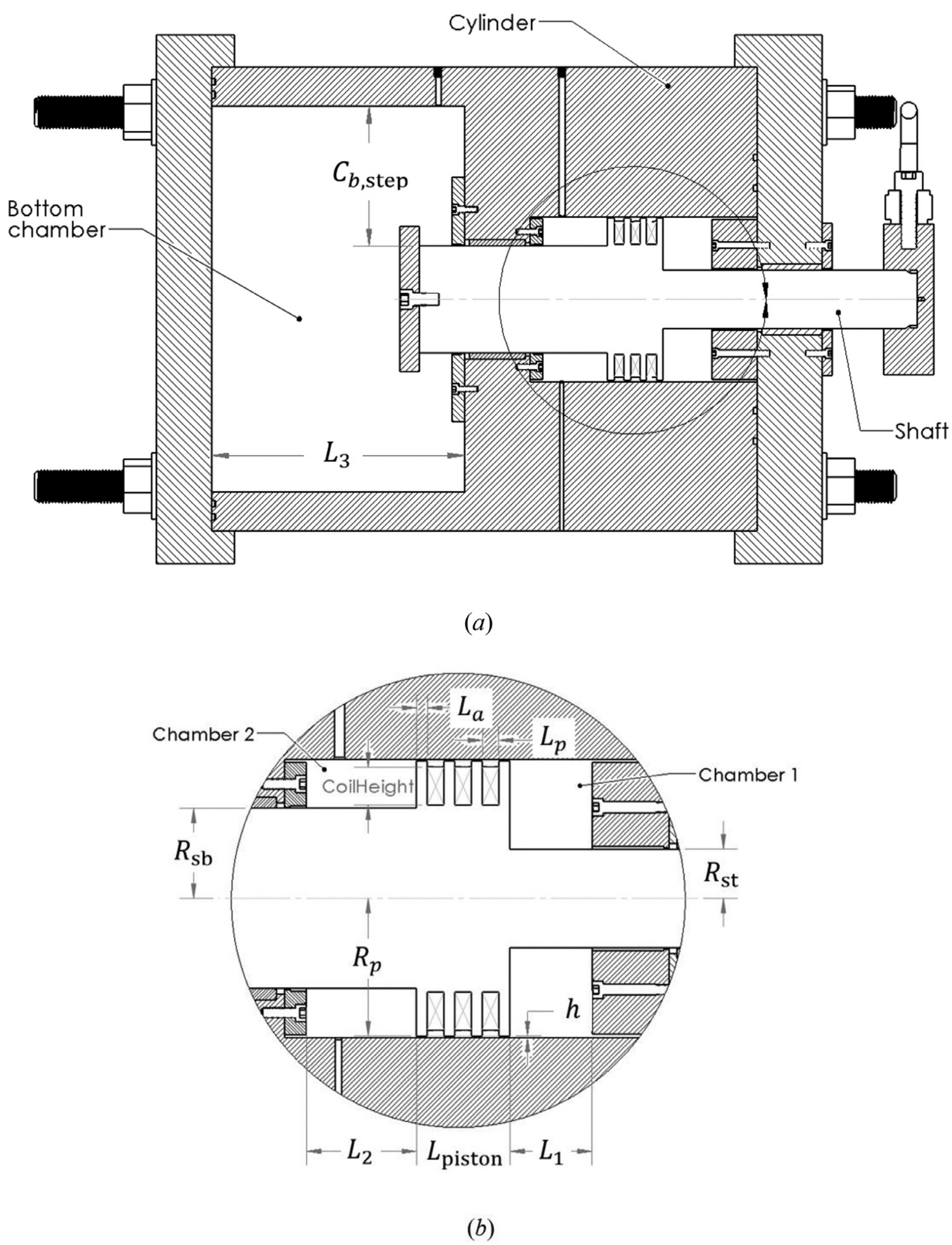

Fig. 4. Significant geometric design parameters: (a) 2D- cross-section of the BLS-CRMD and (b) close-up view of the upper chamber.

2.3. Finite element modeling

This section discusses the structural, electromagnetic, and thermal analyses. The model geometries here are drawn based on optimized geometric parameters listed later in Section 3. The model was updated iteratively during the design process to reach the design targets. In general, an FEA involves uncertainties arising from the modeling assumptions, discretization schemes, and computation (or truncations) errors. These uncertainties can be categorized under two broader groups: aleatory and epistemic [47]. The aleatory uncertainties are related to the randomness of the variables governing the computational solution such as material properties, whereas the epistemic ones are more related to obscurities in the definition of the computational model. In this study, every effort was made to minimize both types of uncertainties. Specifically, at least two (up to four) software were used for each single type of physics simulations to minimize the epistemic uncertainties. Further, the related built-in material properties in the material libraries of the software were updated based on the information obtained from the original material manufacturers. Also, particular care was exercised to ensure that the solutions were mesh independent. All these practices ensured that the FEA results were dependable before moving forward with the fabrication of the device.

2.3.1. Structural analysis

Three-dimensional structural Finite Element Analysis (FEA) of the BLS-CMRD – subjected to loads and boundary conditions imposed by the experimental setup (Fig. 18 Figure 20) – was performed by using Ansys software. Because the assembly was symmetric, only half of the assembly was physically modeled with appropriate boundary conditions. The model was further reduced according to the regions of stress concentrations to save on computer resources and computational time (Fig. 6). After generating the model, a corresponding material was assigned to each component. AISI 1018 steel was chosen for the shaft and cylinder material due to its good magnetic properties. The top cap, top pedestal, and shaft stopper were made from A36 (mild steel). The bearings were made from oil-impregnated sintered bronze alloys. The bottom bearing

Table 2
Optimized Input and Output Parameters at $T = 25$ °C.

Input parameters		Output parameters		
h	0.0015 m	Eq. (1)	D	2.60
R_p	0.125 m	Eq. (2)	k_c	6.318 kN/m
			k_r	25,671 kN/m
L_a	0.010 m	Eq. (14)	ζ viscous	0.17
L_p	0.015 m		Min. FOS (Shaft)	2.50
R_{st}	0.045 m		Max. shear deformation (Shaft)	0.21 nmi
R_{sb}	0.082 m		F_f	5500 N
L_1	0.075 m	Eq. (6)	$F_{viscous,r}$ ($X = 25.4$ nun and $F = 4$ Hz))	72,932 N
L_2	0.100 m		$F_{viscous,c}$ ($X = 25.4$ mm and $F = 4$ Hz))	31,466 N
L_3	0.320 m	Eq. (8)	$F_{MR,r}$ (for $\tau = 40$ kPa))	123,960 N
$C_{b,step}$	0.215 m		$F_{MR,c}$ (for $\tau = 40$ kPa))	81,130 N
w	0.790111 m			
Q_r	0.027275 m^3/s			
Q_c	0.017851 m^3/s			
β_{MRF} (assumed)	0.748 GPa			
$\beta_{Silicone}$ (assumed)	1.13 GPa			
$A_{s,r}$	0.014762 m^2			
$A_{s,c}$	0.021124 m^2			
V_r	0.006308 m^3			
V_c	0.083596 m^3			
$A_{p,r}$	0.042726 m^2			
$A_{p,c}$	0.027963 m^2			
L_{piston} ($3L_p + 4\ L_a$)	0.085 m			
L ($4L_a$)	0.040 m			

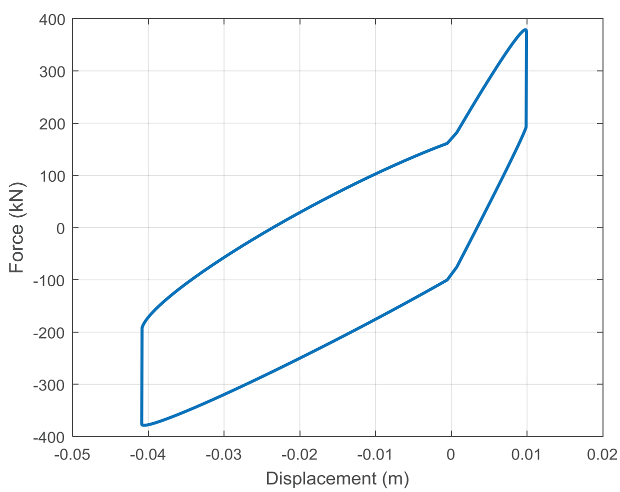

Fig. 5. Total device force vs. displacement curve of BLS-CMRD for a sinusoidal input of 0.0254 m at 4 Hz, and 1 A.

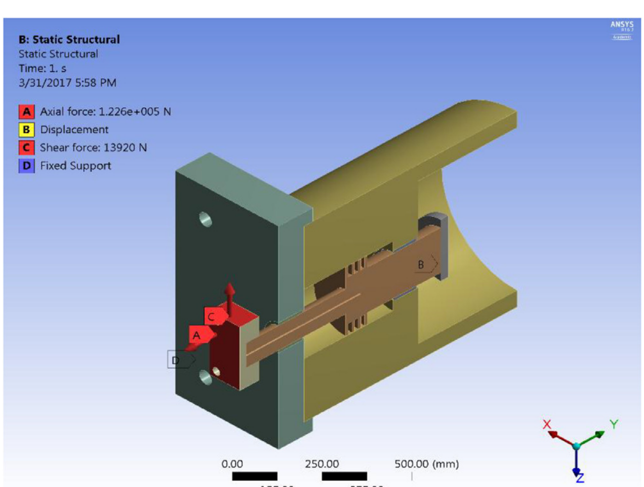

Fig. 6. Ansys FEA model with loading and boundary conditions.

was selected to be Oilite bronze® (SAE 841) because the force demand to this bearing was relatively small. The top bearing was, however, chosen to be Super Oilite® (SAE 863) as it was subjected to high compression stresses from the vertical shear loading.

After the material selection, the loadings and boundary conditions were assigned appropriately to represent the physics of the device. For the rebound mode, a 122.60 kN axial load and a 13.92 kN shear load were applied on the front and top faces of the top pedestal, respectively. Also, a 14 MPa hydrostatic pressure was applied to the inner surface of the upper chamber based on the values listed in Table 2. Fixed support boundary conditions were applied to the screw holes on the side of the top cap. A displacement boundary condition with $(x,y,z) = (\text{free},0,\text{free})$ was assigned to the shaft stopper. All connections between the parts were modeled to reflect the real operating conditions of the device. For instance, because the shaft oscillated through both the top and bottom bronze bearings, frictional contacts were assigned to the connections between the shaft and the top and bottom bronze bearings with a friction coefficient of 0.13. The connections between the bearings and the cylinder were defined as bonded contacts since both bearings were press-fitted to the cylinder. The connection between the cylinder and the top cap was defined as a frictional contact with a friction coefficient of 0.2. Finally, the connection between the shaft and the top pedestal was defined as a bonded contact since the top pedestal was screwed on the shaft, and the threaded connection strength was evaluated analytically.

Simulation results were investigated for the minimum FOS over the entire device, and the maximum total displacement on the shaft as per the design requirements listed in Table 1. Fig. 7 shows the results for the FOS and the total displacement. The FOS is minimized on the top bronze bearing where it is compressed against the top cap by the shaft. The displacement is maximized on the top pedestal, and reduces gradually along the shaft axis. A mesh independency analysis with Ansys built-in tool was conducted to ensure that the solution converged to a constant as the number of mesh elements was increased. After the mesh independency analysis, the minimum FOS was determined to be 2.48 on the top bronze bearing, and the maximum shear displacement on the shaft was found to be 0.21 mm.

A parametric study was conducted to investigate the variations of minimum FOS and maximum shear displacement with the geometric dimensions of the device. The radius of the shaft, R_{st} was found to be the controlling parameter for both FOS and maximum shear displacement,

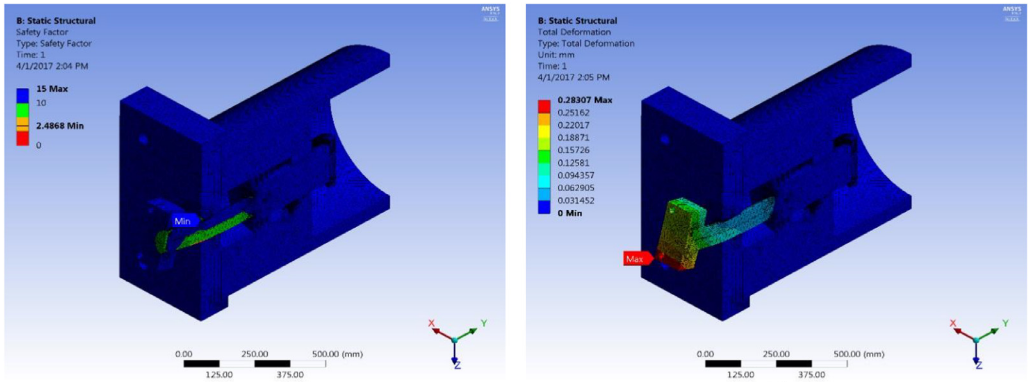

(*a*) (*b*)

Fig. 7. FEA results: (a) minimum FOS and (b) maximum total displacement (displacements are magnified by 310%).

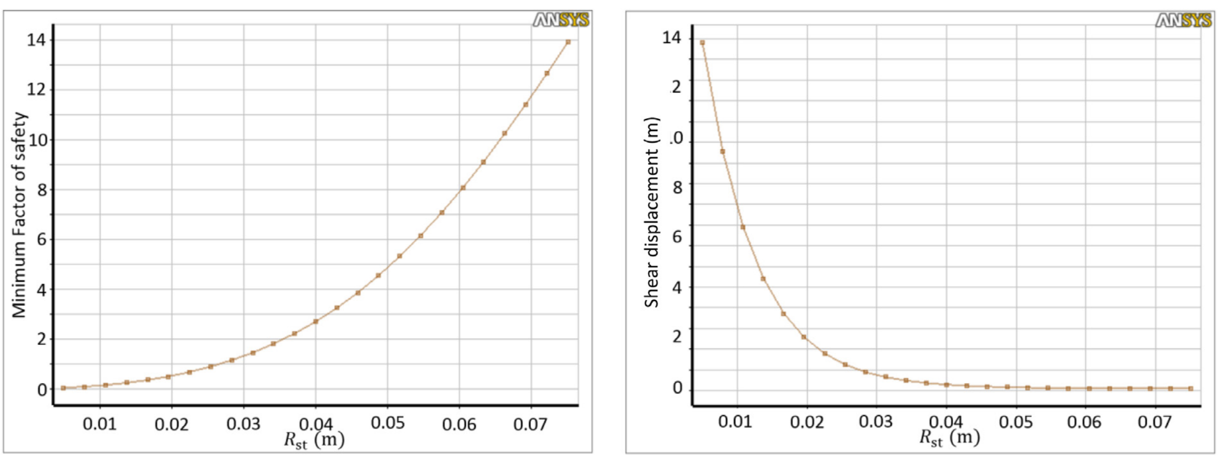

(*a*) (*b*)

Fig. 8. Variations of the minimum FOS and maximum shear displacement with the radius R_{st} of the top shaft.

as shown in Fig. 8. As the radius of the shaft was increased, the FOS is observed to increase, while the maximum shear displacement decreased, exponentially.

2.3.2. Electromagnetic analysis

The MR valve generates the required viscous damping ratio, $\zeta_{viscous}$ and determines the dynamic range, D. As mentioned previously, the valve allows the flow of the MR fluid through the flow channel, which provides a passive damping when no magnetic field is applied and a semi-active damping when a magnetic field is applied to the MR fluid. D (Eq. (1)) requires a value for F_{MR}, which is a function of the dynamic yield stress, $\tau(B)$ of the MR fluid, where B is the magnetic flux density developed in the flow channel. For an electromagnet, B is given by,

$$B = \mu\left(\frac{N}{L_c}\right)I \tag{10}$$

where μ is the magnetic field permeability of the material, N is the number of turns of the coil, L_c is the axial length of the coil, and I is the current applied to the coil. The MR valve and the representative magnetic flux lines are shown in Fig. 1*b* and *c,* respectively. The Maxwell module in Ansys was used to calculate B in the flow gap. The BLS-CMRD was composed of cylindrical components except the top and bottom caps, and top pedestal. Because these parts were square and were also far from the magnetic field region, they could be approximated to be cylindrical without a loss in the accuracy of the analyses. Therefore, the analyses were applied to a 2D axisymmetric model for efficiency. The axisymmetric model is shown in Fig. 9. Figure 10a*,* and b with its main components and modeling assumptions. Although the magnetic field was concentrated around the piston, analyses were applied to a model of the entire device to increase accuracy.

The coils were assumed to be wound in alternating directions to achieve an overall higher magnetic field in the flow channel. The magnetic relationships for the MR fluid (MRF-132DG) are provided as follows [41]:

$$B = 0.68\left[1 - e^{(-10.97\mu_0 H)}\right] + \mu_0 H \tag{11}$$

$$\tau_y = 63,855.60\ \tanh\left(6.33x10^{-6}H\right) \tag{12}$$

where B is the magnetic flux density (in T), H is the magnetic field intensity (in A/m), τ_y is the yield stress (in Pa), and $\mu_0 = 4\pi$ x 10^{-7} T/(A/m). The magnetic characteristics of the MR fluid used in this study are also given in Fig. 9.

Fig. 10 shows the result for magnetic flux density, B on the MR valve for the current input of 2500 Amp-turns. The magnetic field develops in the regions of the MR fluid where it neighbours to the metal parts of piston. The lengths of these regions are called active pole lengths (red regions in the flow gap in Fig. 11), whereas the coil lengths are called passive pole lengths (blue regions in the flow gap in Fig. 11).

The yield stress is found to be varying with the current input as follows:

$$\tau = 44,960\ \tanh(1.108I + 0.2893) \tag{13}$$

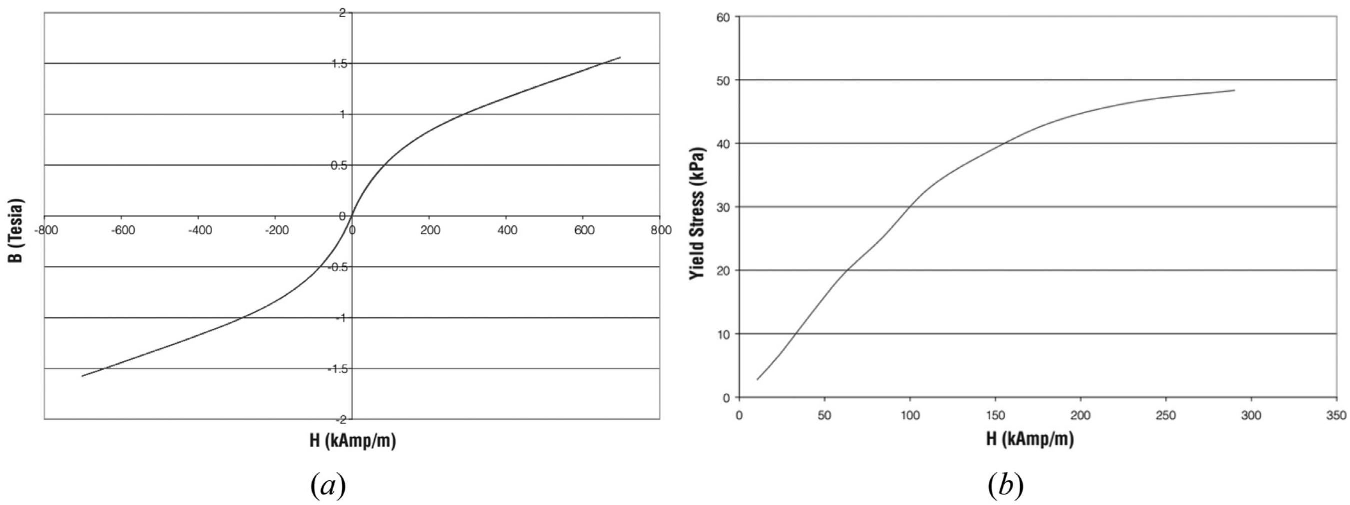

Fig. 9. (a) B-H and (b) τ_y-H curves of the MRF-132DG [41].

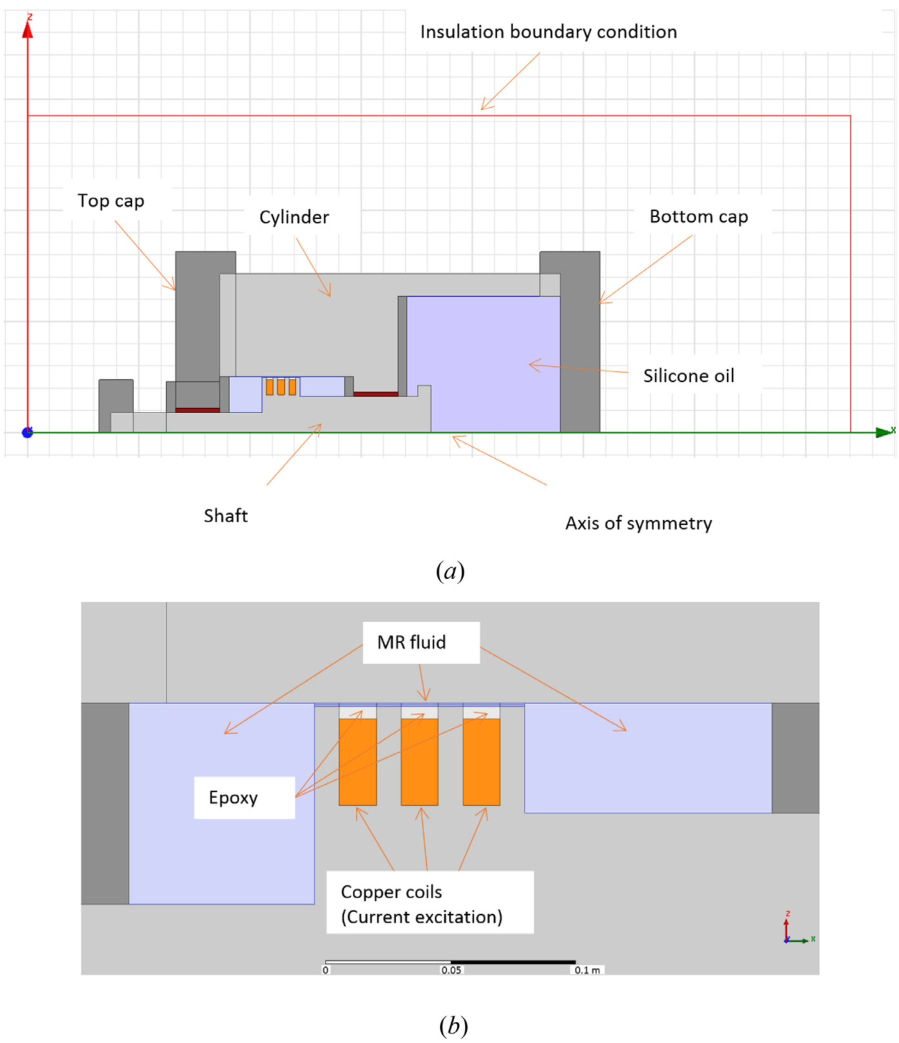

Fig. 10. (a) Axisymmetric model for the electromagnetic analysis in Ansys Maxwell module and (b) detail view of the MR valve.

for one coil of 1135 turns, and I in A. The magnetic field depends on the magnetic properties of the materials as well as the number of turns of the coil and the applied current to the coil. The number of turns (1135) was optimized for a limited power source.

Next, the effects of the geometric dimensions of the MR valve and the applied current on the viscous damping ratio ζ_{viscous} and dynamic range D are investigated. Assuming a simple harmonic excitation, $x(t) = X\,sin(\omega_d t)$, ζ_{viscous} is given by:

$$\zeta_{\text{viscous}} = \left(\frac{W}{\pi\omega_d X^2}\right)\left(\frac{1}{2\sqrt{km}}\right) \tag{14}$$

where $W = \int_0^{2\pi/\omega_d} F_{\text{viscous}}\,dx$, m is the mass, k is the spring constant, ω_d and X are the driving frequency and amplitude of the harmonic excitation, respectively. D was given Eq. (1) and is restated here for conve-

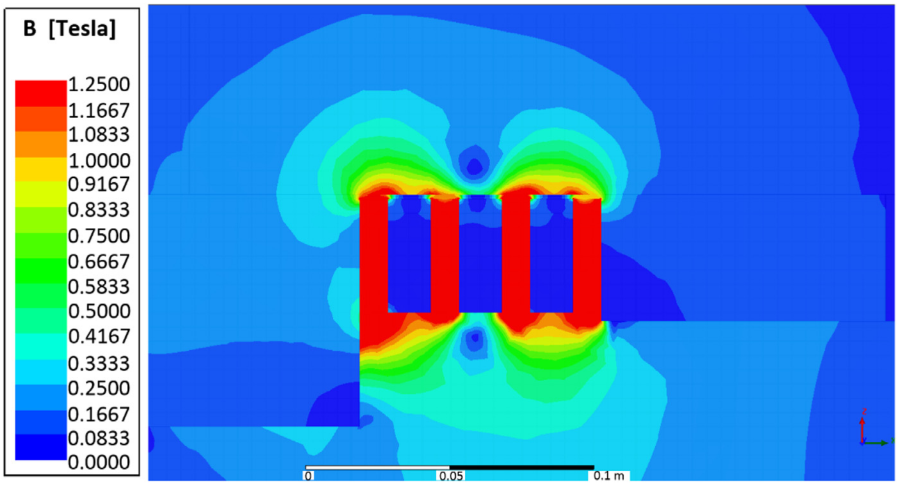

Fig. 11. Magnetic flux density, B distribution after an electromagnetic analysis for the current input of 2500 Amp-turns.

nience:

$$D = \frac{F_{\text{damper}}}{F_{\text{uncontrollable}}} = \frac{F_{\text{MR}} + F_{\text{viscous}} + F_{\text{friction}}}{F_{\text{viscous}} + F_{\text{friction}}} = 1 + \frac{F_{\text{MR}}}{F_{\text{viscous}} + F_{\text{friction}}} \tag{15}$$

F_{viscous} appears in both Eqs. (14) and (15), which makes ζ_{viscous} and D related to each other. Fig. 12 shows the variations of ζ_{viscous} and D with respect to the height of the flow gap, h, active pole length, L_a, passive pole length, L_p, radius of the piston, R_p, and the current input. Each parameter was varied within the range shown in the graphs, while the remaining parameters were set to the optimized values presented later in Table 2.

To achieve higher D's, F_{MR} must be maximized while F_{viscous} is minimized, since F_{friction} is usually constant within a range as suggested by Eq. (1). However, as given by Eqs. (6) and (8), F_{viscous} and F_{MR} are both functions of h, L_a, L_p, and R_p. Noting that F_{friction} is constant and keeping all other parameters constant, ζ_{viscous} greatly decreases with increasing values of h, as F_{viscous} is inversely proportional to h (Fig. 12b). For small h, F_{viscous} decreases two orders of magnitude faster than F_{MR} with increasing values of h, and thus, leads to increasing D.

Increasing L_a, increases F_{MR}, and thus, increases D in two ways (Fig. 12c). First, increasing L_a increases the magnetic field generated in the flow gap, the dynamic yield stress, $\tau(B)$, and thus, F_{MR} since $\tau(B)$ is a multiplier in Eq. (8). The increase in $\tau(B)$ is limited by the magnetic saturation of the MR fluid. Second, increasing L_a directly increases F_{MR} since L_a is a multiplier in Eq. (8). ζ_{viscous}, on the other hand, increases linearly with increasing L_a as it increases the axial length of the piston, L_{piston}, which is a multiplier in F_{viscous} (Eq. (6)). The variation of ζ_{viscous} with L_a is shown in Fig. 12d.

The dynamic force range, D decreases with increasing passive pole length, L_p as shown in Fig. 12e. This is because as L_p increases, the length of the piston increases and F_{viscous} increases, resulting in lower D. On the other hand, ζ_{viscous} increases linearly with increasing L_p since it increases the axial length of the piston, L_{piston}, which is a multiplier in F_{viscous} (Eq. (6)). The variation of ζ_{viscous} with L_p is shown in Fig. 12f.

Increasing R_p decreases D because F_{viscous} increases two orders of magnitude than F_{MR} with R_p (Fig. 12g). ζ_{viscous} increases with increasing R_p values as shown in Fig. 12h, since R_p is a direct multiplier in Eq. (6).

Increasing current input to the coils increases the magnetic field generated in the flow gap and thus, F_{MR} leading to increasing D. This increase is limited by the magnetic saturation of the MR fluid. Therefore, increase in D gradually levels off (Fig. 12i). Finally, ζ_{viscous} is not affected by the applied current because F_{viscous} results from passive fluid friction only (Fig. 12j).

In summary, the combination of h, L_a, L_p, and R_p can be optimized to reach the given targets for ζ_{viscous} and D. Optimal values of the parameters were determined based on the integrated analysis within Ansys, presented later in Section 3.

2.3.3. Thermal analysis

Temperature has been a concern in the design of MR fluid devices as it deteriorates their performances [48–51]. In the current design, the total energy dissipation is a direct heat source to the MR fluid in the upper chamber. This manifests itself as an increase in the temperature of the fluid. The elevated temperatures affect the performance of the BLS-CMRD in several ways. Most importantly, seals might be damaged with increased temperature. McKee et al. [51] demonstrated the effects of temperature on the performance of seals. They showed that the seals expand with increasing temperature, which causes additional compression and thus, deformation on the seals. They reported that the seals failed suddenly and unexpectedly during testing when the temperature was raised to around 80 °C. Also, before the failure occurred, the expansion on the seals caused an increase in the friction force because the seal lips pushed stronger against the shaft surface. The MR fluid also expands with elevated temperatures, which results in pressure buildup inside of the chamber. The added pressure pushes the seals against the shaft surface more strongly, which also causes an increase in the friction force. The temperature rise also affects the properties of the MR fluids. Both the bulk modulus and viscosity of the MR fluid decrease with the increased temperature, reducing the stiffness and damping, respectively. Temperature increase is also known to degrade the magnetic properties of the MR fluids. According to Curie's law, the iron particles inside the MR fluid partially lose their ability to be magnetized.

Electromagnetic heating, produced by the copper coils, is another heat source in the system. When activated, current flows through the copper wires. Although copper has a high electrical conductivity, resistance to electrical current causes Ohmic power losses. This phenomenon is also known as Joule-Lenz effect. The Ohmic losses are transformed into heating, which is often called Joule heating. The Joule heating raises the temperature of the coils, as well as the surroundings. As the temperature in the coils rise, the resistance of the wires increases further. Additional power is required for the coils to maintain the same magnetic field in the MR fluid. Based on Curie's law, the valve piston and the cylinder wall also partially lose their magnetic properties with increasing temperature. The heat transfer to the piston and the cylinder wall from both the MR fluid and coils consequently reduces the efficiency of the electromagnet. These heating considerations have to be taken into account in the design of a BLS-CMRD.

To assess the effects of heating on the performance of the BLS-CMRD, a thermal analysis was conducted using Ansys software. The thermal analysis is based on theoretical calculations to determine the heat generation due to viscous dissipation, as well as an electromagnetic analy-

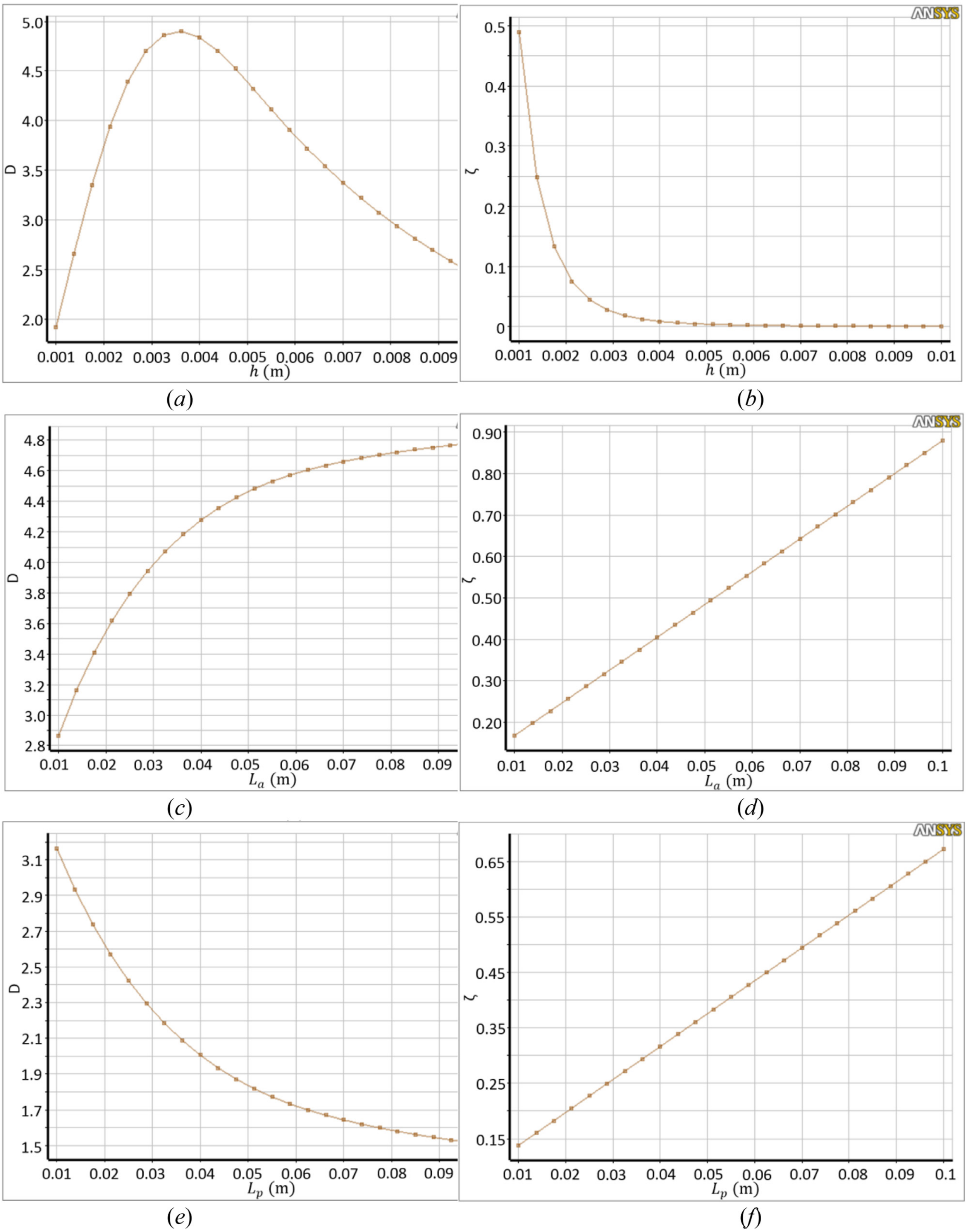

Fig. 12. Variation of dynamic force range, D and viscous damping ratio, ζ_{viscous} with respect to the (a)-(b) flow gap, h, (c)-(d) active pole length, L_a, (e)-(f) passive pole length, L_p, (g)-(h) piston radius, R_p, and (i)-(j) current input.

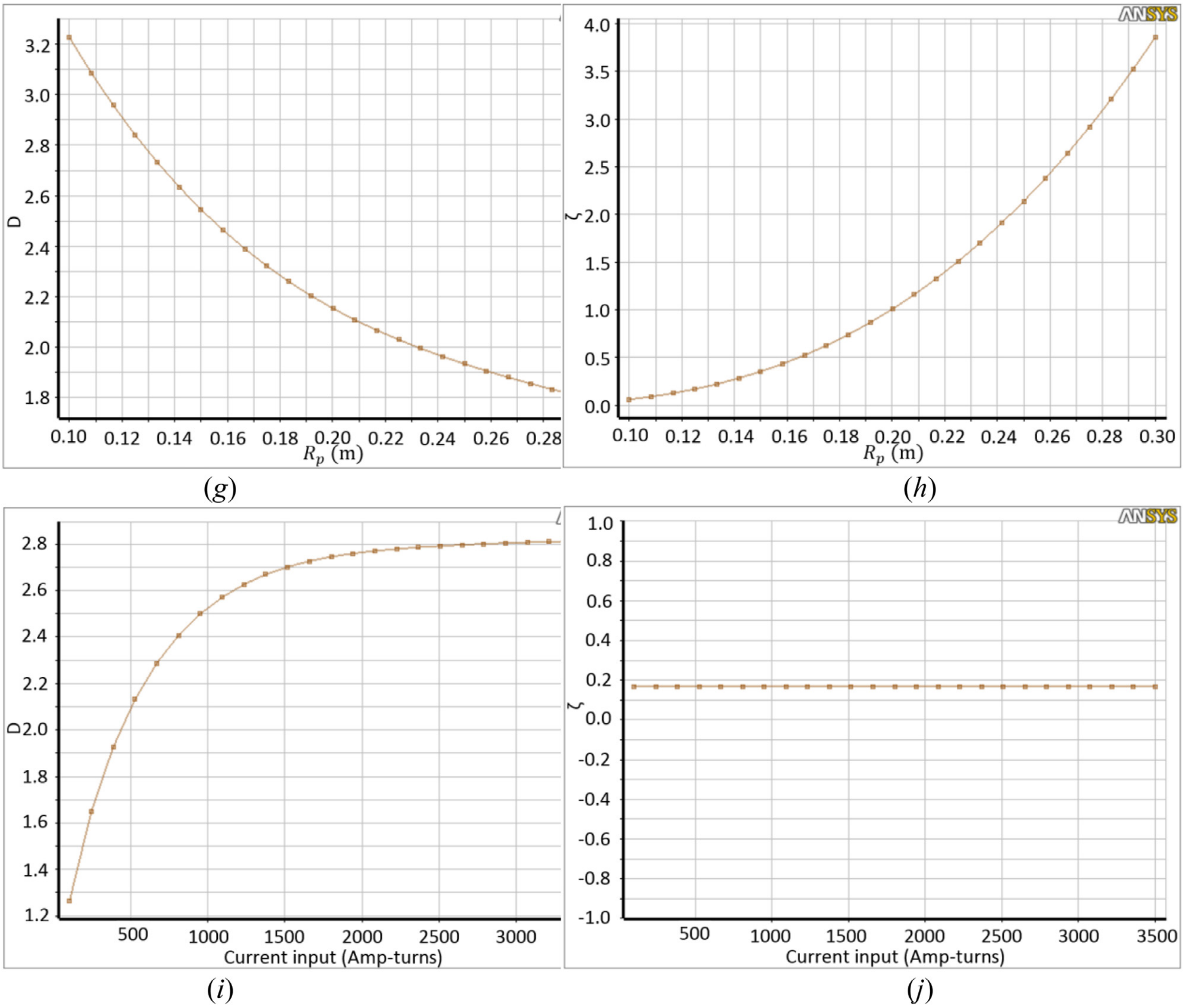

Fig. 12. Continued

sis to calculate the heat generation from Joule heating. The theoretical calculations were performed in Excel module, whereas the electromagnetic analysis was performed in Maxwell module. The computed heat sources were then input to the Transient Thermal module. Following the heating analysis, a cooling analysis was conducted to calculate the time required for the MR fluid to cool down to the room temperature to achieve consistency between the tests. During the analyses, the system was considered to operate at its upper limit conditions, i.e., the maximum stroke, maximum frequency, and maximum applied current, to ensure the maximum heat generation in the system. Fig. 13 shows the schematic of the program developed in Ansys.

Fig. 14 shows the heat loads and boundary conditions used in the Transient Thermal analysis. Although the top and bottom caps are square, the system was modeled as axisymmetric because the cylinder, shaft, and seal glands are all axisymmetric, as was shown in Fig. 1. The total energy dissipation was obtained by the superposition of energy dissipations associated with the friction, viscous, and MR damping as:

$$W_{\text{total}} = 4F_{\text{friction}}X + \pi F_{\text{viscous}}X + 4F_{\text{MR}}X \tag{16}$$

in the Excel module and was input to the Transient Thermal module as a heat source (labeled as A in Fig. 14). Here X is the peak displacement to consider the limit conditions for the energy dissipation, and F_{friction}, F_{viscous}, and F_{MR} were previously described in Eqs. (4), (6), and (8), respectively. The calculation of the MR damping force requires the information of the magnetic flux density in the flow gap. This information was passed to the Excel module from the Maxwell module. The Joule heating was, on the other hand, obtained by the Maxwell module and transferred to the Transient Thermal module. This was verified using the theoretical equation for Joule heating, $\dot{Q} = I^2R$, where I is the current applied to the coils, and R is the resistance of the coils (labeled as B in Fig. 14). The system was assumed to be cooled by a fan at room temperature during the tests. The external effects were represented by a convection boundary condition with $T_\infty = 22°\text{C}$ and $h = 50\,\text{W/m}^2\,°\text{C}$ assigned to all outer surfaces of the system (labeled as C in Fig. 14).

The maximum temperature was found to be around 42.5 °C in the centers of Chamber 1 and 2. Because the cylinder wall of the upper chamber was very thick (0.23 m), heat was not able to escape, and became mostly trapped in Chamber 1 and 2. The maximum temperature increased linearly at a rate of about 4 °C/s. Analyses were repeated for different strokes, frequencies, and currents. The stroke, frequency, and current input were varied from 0.00635 to 0.02540 m, 0.5 to 4 Hz, and 100 to 3,500 Amp-turns, respectively. Fig. 15 shows the variations of the maximum temperature with these three parameters as a result of the Transient Thermal analysis after 5 s of continuous cyclic loading. For each case, the third parameter was fixed at the median of its range. The maximum temperature was observed to increase linearly with increasing

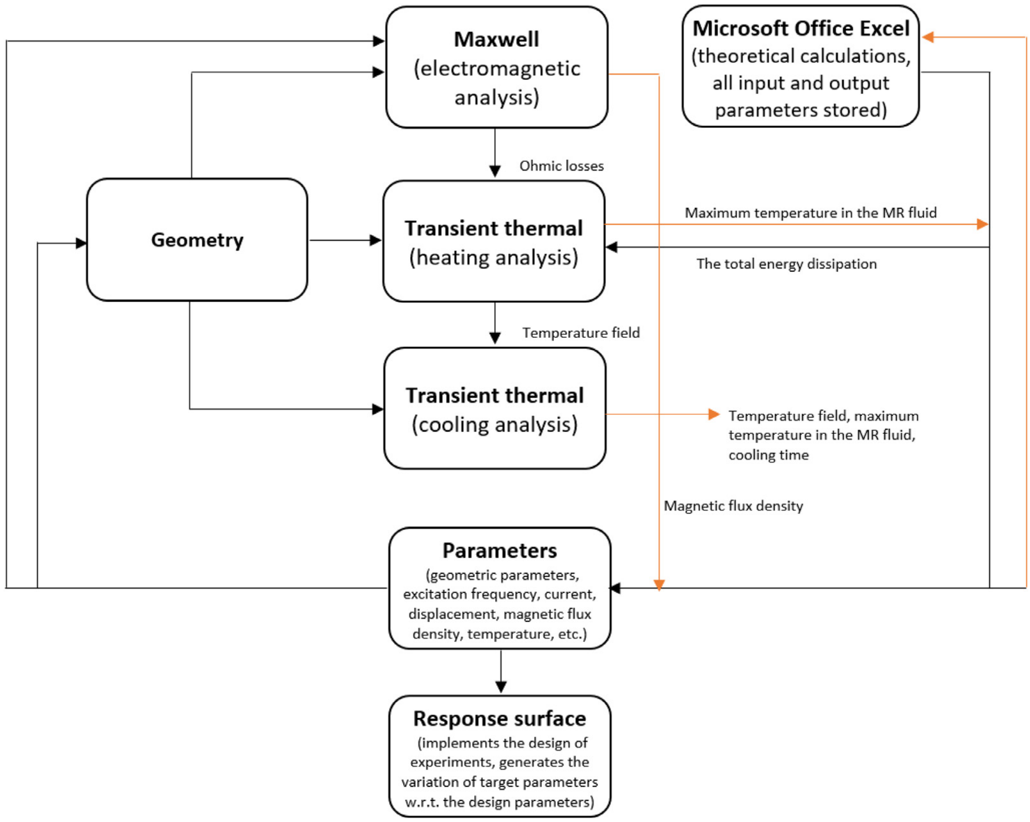

Fig. 13. Analysis program developed in Ansys, showing the connections between the electromagnetic (Maxwell module), thermal (Transient thermal module), and theoretical formulations (Excel module).

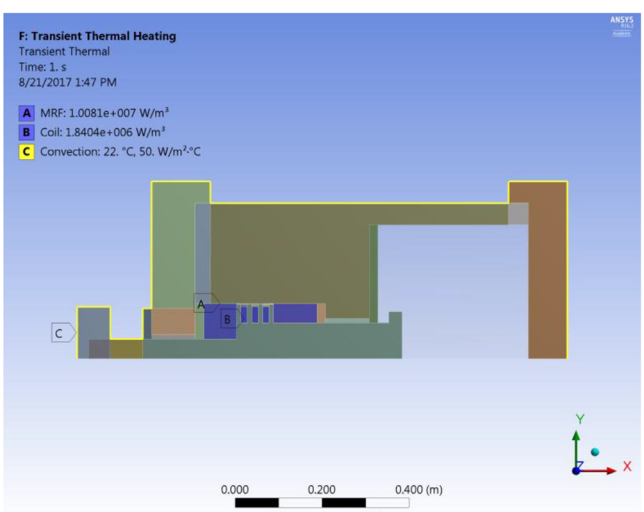

Fig. 14. Heat loading and boundary conditions for the Transient Thermal heating analysis.

stroke and frequency. The temperature was also found to increase with increasing current and level off as the current reached around 2,000 Amp-turns. This leveling off occurred because the MR damping force saturated, causing the energy dissipation to reach its limit.

As mentioned previously, another thermal analysis was conducted to obtain the time required to cool the system down to room temperature. To do this, the maximum temperature found in the Transient Thermal analysis was assigned to the MR fluid as an initial temperature, and all the outer surfaces of the system were subjected to convective boundary condition with $T_\infty = 22°C$ and $h = 50\,W/m^2\,°C$ to reflect the device being cooled by a fan at room temperature. Fig. 16 shows the temperature contours after 1 h. The maximum temperature was found to be concentrated in Chamber 1, which has a higher volume of MR fluid than Chamber 2. The heat flowed through the cylinder wall of the lower chamber rather than the silicone oil, because the steel AISI 1018 has a higher thermal conductivity than that of silicone oil. The variation of the maximum temperature with time is also plotted in Fig. 17. The maximum temperature was found to decrease exponentially, and it was predicted to take almost one hour for the device to cool down to the room temperature.

The temperature also affects the physical properties of the MR fluid. The viscosity of the MR fluid is known to decrease exponentially with increasing temperature according to the following formula [41],

$$\mu(T) = \mu_{@40\ (°C)}\ (\mathrm{Pa})e^{\left[\frac{(1+2.43\phi)(40\ (°C)-T\ (°C))}{(T\ (°C)+48\ (°C))}\right]} \tag{17}$$

where $\mu_{@40\ (°C)} = 0.112$ Pa•s and $\phi = 0.32$ for the MRF-132DG (also given in Fig. 19). The bulk modulus of the MR fluid, β also decreases linearly with increasing values of temperature as shown by [41] with the following relation,

$$\beta(T) = 0.735x10^9(\mathrm{Pa}) - 0.267x10^7\left(\frac{\mathrm{Pa}}{°\mathrm{C}}\right)\left(T(°\mathrm{C}) - 22(°\mathrm{C})\right) \tag{18}$$

To examine the effects of temperature on the design requirements of the viscous damping ratio, ζ_{viscous} dynamic force range, D, and rebound stiffness, k_r, Eqs. (17) and (18) were implemented into the Excel module in the Ansys program. Fig. 18 shows the effects of temperature on these three design requirements. ζ_{viscous} was found to decrease exponentially as the temperature increases (Fig. 18a), because the viscosity of the MR fluid decreases exponentially with temperature according to Eq. (17). D is observed to increase with increasing values of temperature (Fig. 18b). However, the rate of increase reduces at higher temperatures,

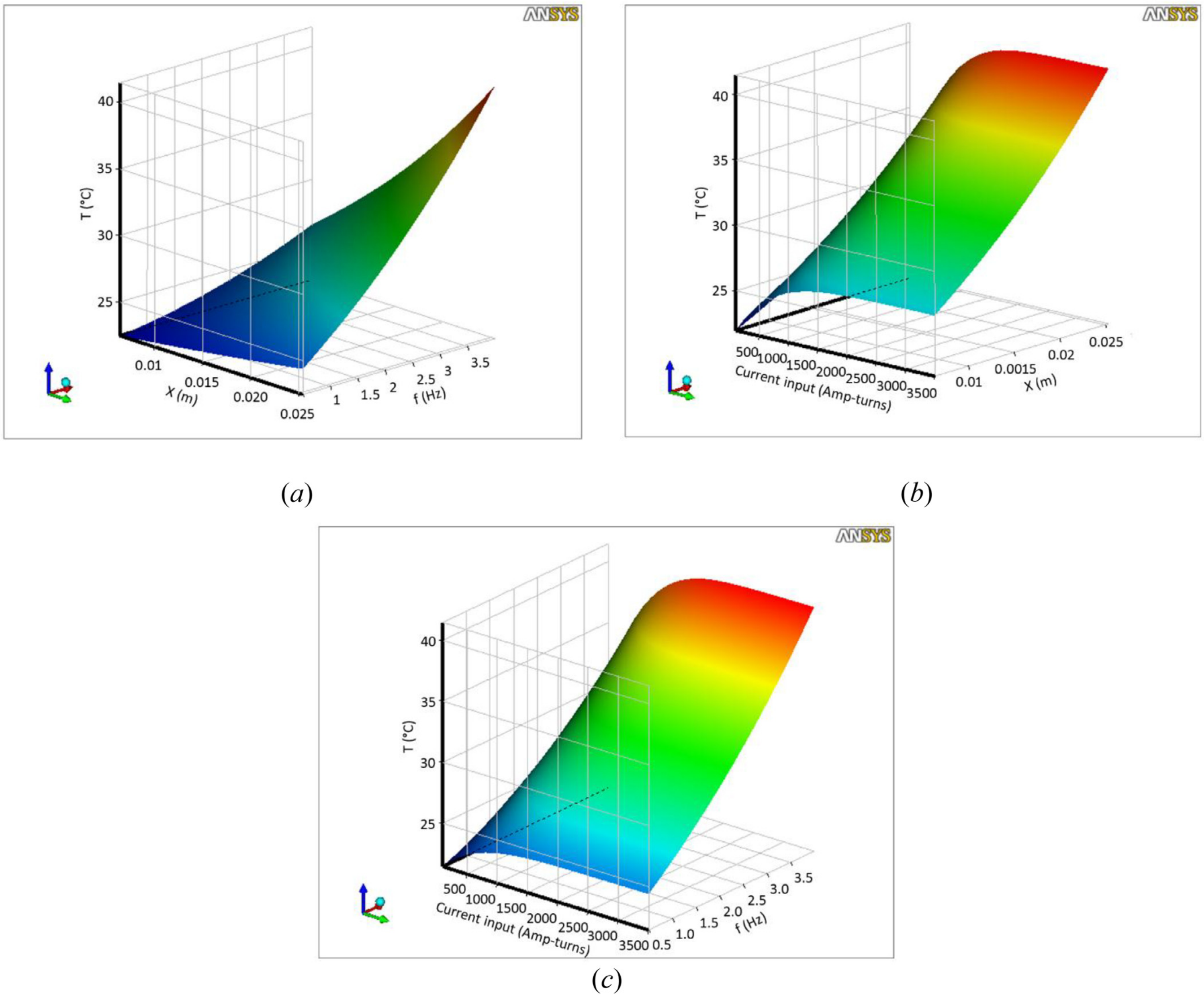

Fig. 15. Variations of the maximum temperature in the MR fluid with respect to the stroke, frequency, and current input, for (a) constant current = 1,750 Amp-turns, (b) constant frequency = 2 Hz, and (c) constant stroke = 0.0127 m.

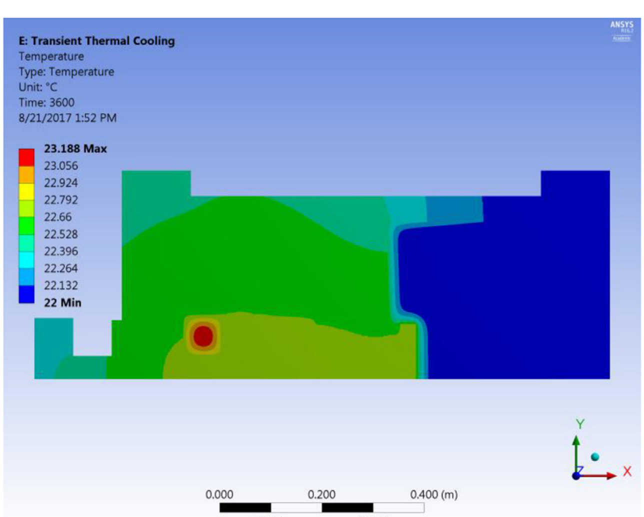

Fig. 16. Temperature distribution after the Transient Thermal cooling analysis.

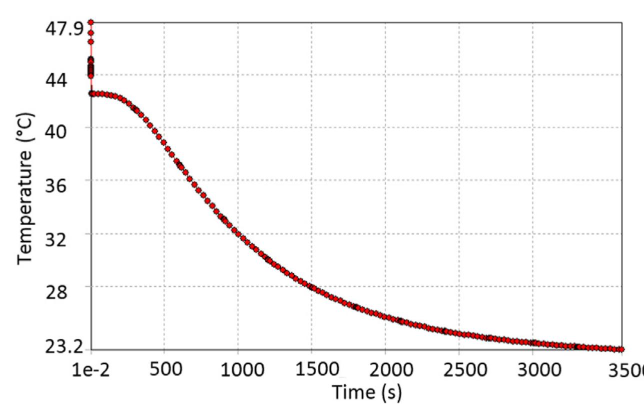

Fig. 17. Variation of the maximum temperature in the MR fluid when the system was subjected to forced cooling with a fan at room temperature.

because F_{viscous} decreases exponentially with increasing temperature according to Eq. (17). Lastly, the rebound stiffness, k_r, decreases linearly with increasing temperature, because the bulk modulus of the MR fluid, β, decreases with increasing temperature according to Eq. (18). As the

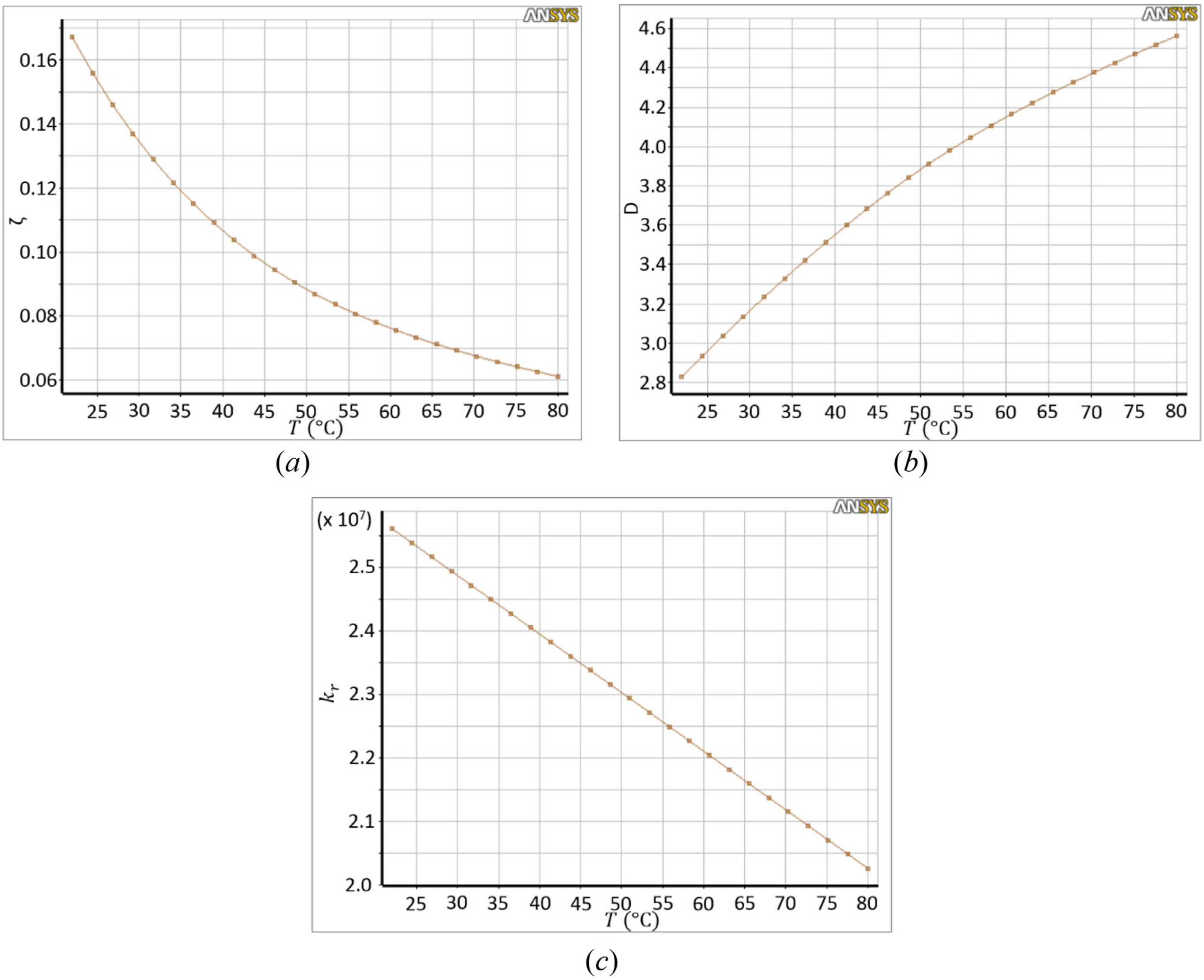

Fig. 18. Effects of temperature on (a) the viscous damping ratio, ζ_{viscous}, (b) dynamic force range, D, and (c) rebound stiffness, k_r.

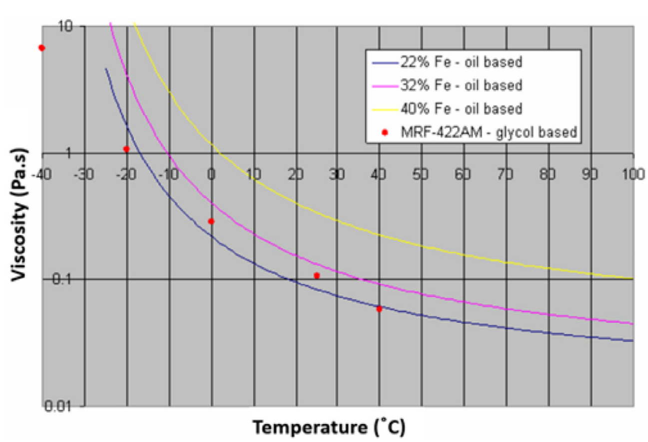

Fig. 19. Variation of the viscosity of the MR fluids of Lord Co.%32Fe – oil based represents the MR fluid used in this study [41].

temperature rises from 22 °C to 42.5 °C, ζ_{viscous} decreases by 45%, k_r decreases by 8%, and D increases by more than 25%.

Considering these findings and the concerns about the performances of the seals and the electromagnet at elevated temperatures, efforts were made to limit the temperature in the MR fluid during the tests. The load duration (3 cycles per trial) was selected to ensure that the maximum temperature did not exceed 25 °C. The temperature was monitored in real-time during the testing using a thermocouple.

3. Design optimization

There have been many studies performed about the optimal design of MR dampers in the literature. Gavin et al. optimized a multi-coil MR damper for the minimal power consumption and inductive time constant [52]. Nguyen et al. studied the optimal MR valve design under geometric constraints [53]. In other studies, Nguyen et al. investigated the optimal design of an MR damper for the target design parameters of damping force, dynamic range, and the inductive time constant [54,55]. Parlak et al. [70] carried out a finite element analysis- and computational fluid dynamics-based optimization study to determine the target damping force of an MR damper and the maximum flux density in its MR valve. Mangal and Kumar demonstrated an optimization procedure for the optimal geometry of MR dampers based on the design of experiments and finite element methods [56]. More recently, Zhang et al. proposed an optimization procedure for a novel one-way pumping MR damper by using FEMM, Matlab, and Isight software to optimize the damper's magnetic system for the desired damping force and dynamic ratio [57]. However, the optimization scheme presented in this work is different and more comprehensive than all these previous studies. It is different due to the physics involved. The optimization procedure includes not only the electromagnetic and thermal analyses but also the structural

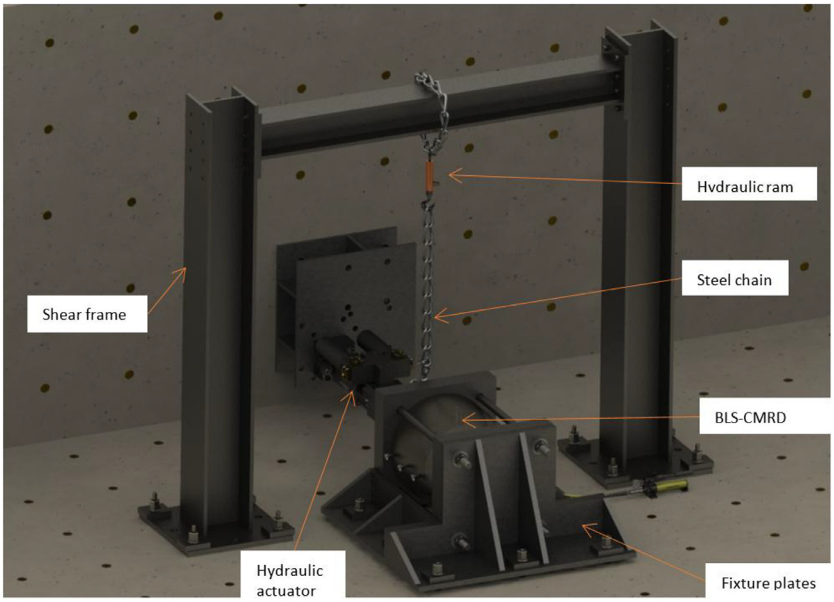

Fig. 20. Solid modeling of the experimental test setup.

analysis. It is the most comprehensible because the target design parameters include not only damping force and dynamic force range but also compression stiffness, rebound stiffness, allowable shear displacement, and minimum structural factor of safety.

The parametric studies in Section 2 reveal that the design values that meet the requirements of Table 1 are controlled by geometric parameters, which were depicted in Fig. 4. In the structural analysis, the minimum FOS and maximum shear displacement were found to depend strongly on R_{st} (Fig. 8). Eq. (2) indicates that the rebound stiffness, k_r, varies with the fourth power of R_{st}. Hence, k_r is also closely related to R_{st}. Also, the electromagnetic analysis shows that D and ζ_{viscous}, are both functions of h, L_a, L_p, and R_p (Fig. 12). Furthermore, the thermal analysis showed that ζ_{viscous}, D, and k_r vary with temperature (Fig. 18).

To achieve the design requirements in Table 1, the parameters R_{st}, h, L_a, L_p, and R_p were optimized while accounting for the temperature effects in ζ_{viscous}, D, and k_r. A multi-objective optimization program was developed in Ansys platform. The program consisted of two stages. In the first stage, the Static Structural and Microsoft Excel modules were run simultaneously to determine the minimum FOS and maximum allowable shear displacement and to calculate k_r and k_c, respectively. In the second stage, the Maxwell, Microsoft Excel, and Transient Thermal modules were run simultaneously to determine the magnetic flux density in the flow gap, to calculate D and ζ_{viscous}, and to account for the heating effects, respectively. The analysis presented previously in Fig. 13 represents the optimization program for the second stage.

The input parameters such as R_{st}, h, L_a, X, f, and current input were transferred from the Microsoft Excel module and were shared with Geometry and Maxwell modules. The Microsoft Excel module not only stored the input parameters but also the output parameters. The analytical expressions, i.e., Eqs. (1)–(4), (6), (8), (9), (12), (14), (16), (17), and (18) were implemented into the Microsoft Excel module as well. The optimum design was explored with the Response Surface Optimization module, where the design of experiments were established, and optimum values were sought. The modules communicated with each other in sequence. For example, the temperature rise in the MR fluid was computed, as follows: The current from Microsoft Excel module was sent to the Maxwell module as an input. The output of the Maxwell module, i.e., magnetic field, H was transferred back to the Microsoft Excel module to calculate $\tau(B)$ Eq. (12)), the various force contributions (Eqs. (4), (6) and (8), and the total energy dissipation, W_{total} (Eq. (16)). Next, W_{total} was transferred to the Transient Thermal module as a heat source to the fluid. Similarly, another output of the Maxwell module, the total Ohmic loss, was transferred to the Transient Thermal module directly as the other heat source to the coils. Then, the Transient Thermal module computed the maximum temperature in the MR fluid as a function of time. The optimized values of input geometric parameters - originally identified in Fig. 4 - and resultant design values are given in Table 2.

4. Experimental validation of the model

The BLS-CMRD was tested at the Large Scale Structures Laboratory of University of Nevada, Reno. A 3D representation of the test set-up is given in Fig. 20. The device was oriented horizontally whereas it would be vertical for the real application. The device was fixed to the laboratory floor by using fixture plates via seven Dywidag tie rods, each capable of providing 355 kN in tension and 71 kN in shear. In order to reflect the real-life loading conditions, the device was excited axially via a 245 kN MTS-244.315 hydraulic actuator sinusoidally, and the shear loading was applied through a 5 ton hydraulic pulling ram attached to a vertical I-beam frame (shear frame).

First the seal friction force were tested at the stroke and frequency of 0.0127 m and 0.01 Hz, respectively. Then, the fail-safe viscous damping forces were characterized at zero current and at different excitation amplitudes and frequencies, ranging from 0.0127 to 0.0254 m and 0.5 to 4 Hz, respectively. Finally, the complete behavior of the BLS-CMRD was characterized at different current inputs, ranging from 0.25 to 1 A, with the same stroke and frequency range above. A comprehensive discussion of the characterization of the device was given in [41].

The theoretical model presented in this study was validated by comparison against the experimental data. Fig. 21 shows the comparisons for different frequency and current levels. The model agreed well with the experimental data. However, the experimental data shows that the force is reduced over a region of the hysteresis loop, referred to as a cut-out region. The cut-out region occurs when the fluid does not flow properly through the flow gap. This is a direct result of entrapped air in the MR fluid. In a cut-out region, the entrapped air is being compressed, and there is no flow through the MR valve. When the air is fully compressed, then the flow starts. The overshoots at the end of the cut-out regions (at the beginning of the flow) in Fig. 21 supports the discussion of no-flow regions. When the air-filled region collapses, the liquid get in sudden contact resulting in a water-hammering behavior, i.e. a local spike in the pressure yielding a local peak in the force values. To remedy the problem, the controllable and passive damping forces were set to be zero in the cut-out regions in Eq. (9). From Fig. 22, it can be seen that the modified model can describe the dynamic response of the device effectively.

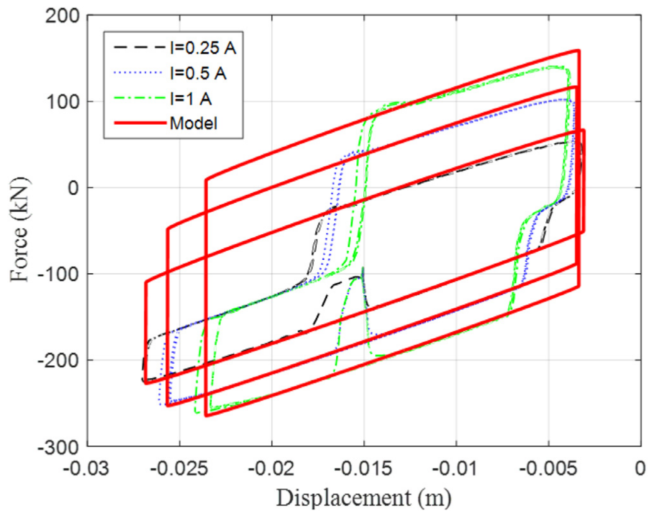

Fig. 21. Comparison of the modeled and experimentally observed force vs. deformation for $X = 0.0127$ m, $f = 1$ Hz, and for different applied currents.

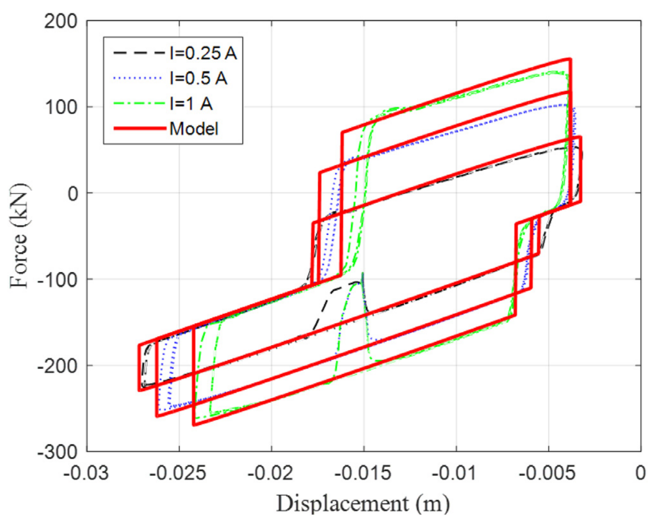

Fig. 22. Comparison of the modified model and experimentally observed force vs. deformation for $X = 0.0127$ m, $f = 1$ Hz, and for different applied currents.

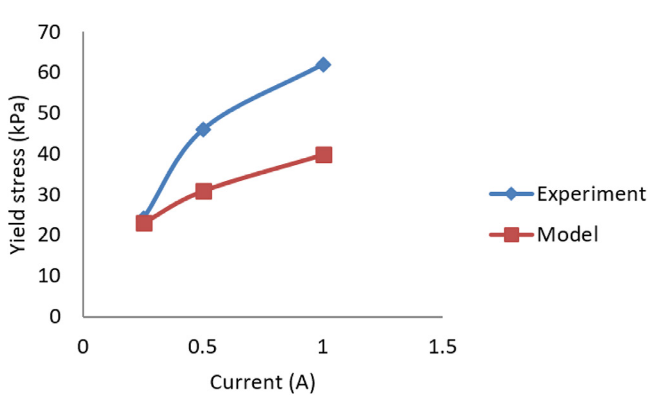

Fig. 23. The experimental and model yield stress vs. current.

The yield stress values were adjusted from the experimental data. Fig. 23 shows the comparison of the model and experimental yield stress values. The deviation in the yield stress values is assumed to be due to the effect of pressure, which is supported by recent studies that showed the yield stress increased under pressure [58–63].

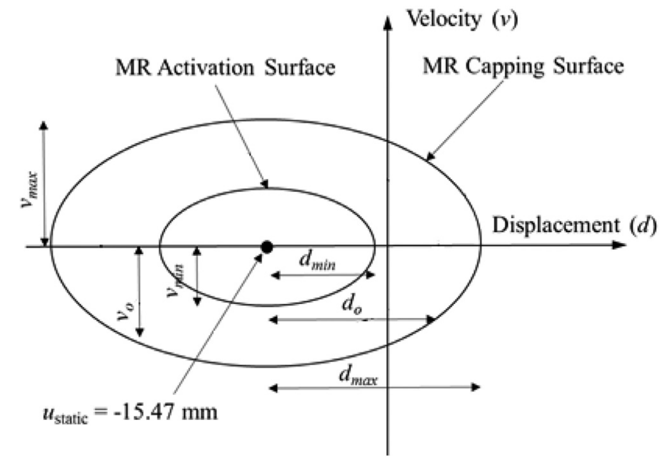

Fig. 24. Device state vector u_z with MR activation surface and MR capping surface.

5. Application of Disp/Vel-based control

To make effective use of the controllable damping offered by the device, a control strategy is needed. A number of studies have evaluated control strategies for MR dampers, such as [58–67]. As part of this research, the authors developed a displacement-velocity based control strategy, and applied it to a 3D rigid block equipped with BLS-CMRDs for vertical isolation, and subjected to earthquake ground shaking. The comprehensive development and evaluation of this strategy is presented in [42,68,69]. Here, the control strategy is summarized briefly, and its application is demonstrated for a single DOF system subjected to sinusoidal motion.

The simplified system considered for this application is a single mass m mounted on the BLS-CMRD described earlier. The equation of motion of the system, when subjected to a vertical ground or base acceleration $a_{gz}(t)$, is:

$$m\ddot{u}_z + c\dot{u}_z(t) + ku_z(t) = -ma_{gz}(t) - (F_{\mathbf{MR}} + F_{\mathbf{friction}}) \tag{19}$$

where u_z is the displacement/stroke history of the BLS-CMRD, c is the viscous damping coefficient (derived from Eq. (6)), k is the instantaneous stiffness of the device (either k_c or k_r from Table 1), and F_{friction} and F_{MR} are determined from Eqs. (4) and (8), respectively.

In the Disp/Vel-based control strategy, the input current to the BLS-CMRD is calculated based on the feedback displacement and velocity of the device. The state of the damper is modeled as a vector valued function of displacement and velocity: $u_z = \{u_z, \dot{u}_z\}$. The input current is varied with the instantaneous magnitude of the vector. The current is activated when a threshold lower bound vector magnitude is reached, and maximum current is applied when a threshold upper bound vector magnitude is reached. These threshold magnitudes are modeled as ellipse surfaces with displacement as the semi-major axis and velocity as the semi-minor axis; d_{min} and v_{min} are the magnitudes of displacement and velocity for the inner ellipse or MR activation surface, whereas d_{max} and v_{max} are magnitudes of displacement and velocity for the outer ellipse, denoted the MR capping surface (Fig. 24). These ellipses are centered at u_{static} and are represented by the following equations:

$$\left(\frac{\mathbf{u_z - u_{static}}}{\mathbf{d_{min}}}\right)^2 + \left(\frac{\dot{\mathbf{u}}_\mathbf{z}}{\mathbf{v_{min}}}\right)^2 = 1\ (\textbf{MR Activation Surface})$$

$$\left(\frac{u_z - u_{\text{static}}}{d_{\text{max}}}\right)^2 + \left(\frac{\dot{u}_z}{v_{\text{max}}}\right)^2 = 1\ (\textbf{MR Capping Surface}) \tag{20}$$

At each instant, the state vector u_z of the device is computed. If the state vector is inside the MR activation surface, no current is applied (passive response). If the state vector is outside of the MR capping surface, the maximum current ($I = 1$A) is applied. For states between the

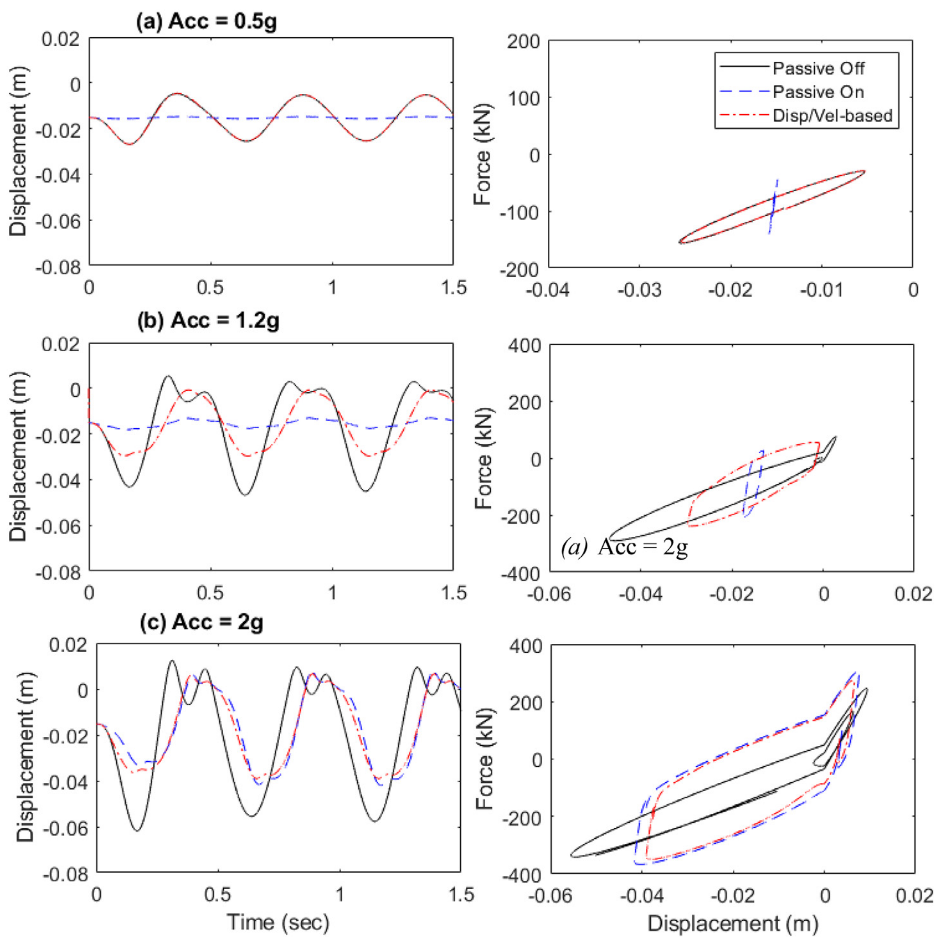

Fig. 25. BLS-CMRD displacement history and force-displacement hysteresis loops for sinusoidal acceleration input: (a) 0.5 g, (b) 1.2 g and (c) 2 g; Disp/Vel-based control compared to Passive-Off and Passive-On schemes.

MR activation and MR capping surface, a partial current is applied. The current varies linearly from zero at the MR activation surface to the maximum at the MR capping surface.

The application of Disp/Vel-based control is demonstrated for the single mass and BLS-CMRD system of Eq. (20). The theoretical parameters of the reduced scale device are used, and the mass is equivalent to a weight of 92.8 kN. Assumed parameters for the MR activation and capping surfaces are: $d_{min} = 0.0125$ m, $d_{max} = 0.0225$ m, and ratio of displacement to velocity or $d/v = 0.07$ s. The system is subjected to sinusoidal input acceleration at varying amplitudes, with frequency $\omega = 12.56$ rad/s or $T = 0.5$ s. (Recall that the fundamental period of the system (based on compression stiffness) is 0.25 s (Table 1). Thus the system is driven at a different frequency to avoid a resonant condition. The response of the system using Disp/Vel-based control is compared to the reference uncontrolled cases: Passive-Off, which means the MR damping force is turned off, and Passive-On, which means a steady current is applied so the MR damping force is always fully present.

BLS-CMRD displacement (stroke) history (left) and force-displacement loops (right) are presented for varying intensity input in Fig. 25. The sequence of increasing acceleration illustrates how the control algorithm responds relative to Passive On and Passive Off. At the lowest input acceleration of 0.5 g (Fig. 25a), the displacement amplitude < $d_{min} = 0.0125$ m (inside the MR activation surface) and only passive damping is present in the hysteresis loop. Thus, Disp/Vel-based control provides identical results to Passive Off, while the Passive On damper is so overdamped that the system cannot seem to initiate movement. At input acceleration = 1.2 g (Fig. 25b), an intermediate current is generated and hence the MR damping is partially activated. For this case, it is seen that Disp/Vel-based control suppresses the displacement significantly relative to Passive On, while the Passive On system remains overdamped. At an input acceleration = 2 g (Fig. 25c), Disp/Vel-based control leads to results similar to Passive On, meaning that the additional MR damping is fully activated. Relative to Passive-On, again the displacement response is suppressed. The MR damping does not become fully activated until large input accelerations because it was designed as a backup system in the event of extreme loading. These examples demonstrate that the controllable damping is effectively utilized to control displacement during increasing intensity motion.

6. Summary and conclusions

In this study, a comprehensive design methodology for a magnetorheological-based isolation system was presented. The modeling approach involved both theoretical and simulation modeling. The theoretical model included four contributions to the BLS-CMRD force: bi-directional liquid spring, friction, passive damping, and semi-active MR damping. The simulation modeling involved structural, electromagnetic, and thermal finite element analyses. The geometric dimensions of the BLS-CMRD were determined via a multi-objective optimization program developed in Ansys platform incorporating both theoretical and simulation modeling.

A prototype of the device was fabricated and subjected to characterization tests. The experimental data generally validated the modeling assumptions. However, the experimental results exhibited cut-out regions in the force vs. displacement that were attributed to the absence of flow through the flow gap in the upper chamber. A modified model was able to capture the device behavior in the cut-out regions effectively. This is rather an assembly issue during the fabrication of the device and could be eliminated with more effective fluid filling procedures. Also, the theoretical shear stress deviated from the experimentally observed shear stress, and should be modified to account for the effect of pressure. A new Displacement/Velocity-based control strategy was applied to a single degree-of-freedom BLS-CMRD with mass system subjected to sinusoidal input acceleration. It was demonstrated that the controllable damping was effectively utilized to control displacement during increasing intensity motion.

In conclusion, the multi-objective design and optimization procedure was effective to meet a challenging set of system requirements for the design of a BLS-CMRD. The control simulations showed that the control strategy was effective to increase the damping as the displacement amplitude increases, and thus control the displacement during higher intensity input. It is believed that this is the first smart damper device that operated under combined lateral and axial loads as large as 28 kN and 245 kN, respectively, which was one of the major design challenges.

Declaration of Competing Interest

None

Acknowledgements

The support from the U.S. National Science Foundation (Grant No. 1437003) was gratefully acknowledged. The authors also extend their thanks to the laboratory staff at LSSL at UNR for their assistance in the development of the device and test setup. Finally, the authors wish to thank Dr. Barkan Kavlicoglu and Advanced Materials and Devices, Inc for their technical support.

References

[1] Reitherman R. Overview of the Northridge Earthquake. In: Proceedings of the NEHRP conference and workshop on research on the Northridge, California Earthquake of January 17, 1994; 1998. p. I-1.
[2] Kircher CA. It makes dollars and sense to improve nonstructural system performance. In: Proceedings of seminar on seismic design, performance, and retrofit of nonstructural components in critical facilities ATC-29-2; 2003. p. 109–19.
[3] Naeim F, Kelly JM. Design of seismic isolated structures: from theory to practice. Design of seismic isolated structures: from theory to practice. New York: John Wiley & Sons, Inc.; 1999.
[4] Taylor AW, Igusa T. Primer on seismic isolation. Reston, VA, USA: ASCE and Task Committee on Seismic Isolation; 2004.
[5] Castaldo P, Ripani M, Lo Priore R. Influence of soil conditions on the optimal sliding friction coefficient for isolated bridges. Soil Dyn Earthq Eng 2018;111:131–48. doi:10.1016/j.soildyn.2018.04.056.
[6] Castaldo P, Palazzo B, Ferrentino T. Seismic reliability-based ductility demand for hardening and softening structures isolated by friction pendulum bearings. Struct Control Health Monit 2018;25:e2256. doi:10.1002/stc.2256.
[7] Kasai K, Mita A, Kitamura H, Matsuda K, Morgan TA, Taylor AW. Performance of seismic protection technologies during the 2011 Tohoku-Oki earthquake. Earthq Spectra 2013;29(S1):S265–93.
[8] Saito T. Observed response of seismically isolated buildings. Response control and seismic isolation of buildings. Higashino M, Okamoto S, editors. New York: Taylor and Francis; 2006.
[9] Moroni MO, Sarrazin M, Soto P. Behavior of instrumented base-isolated structures during the 27 February 2010 Chile earthquake. Earthq Spectra 2012;28(S1):S407–24.
[10] Furukawa S, Sato E, Shi Y, Becker T, Nakashima M. Full-scale shaking table test of a base-isolated medical facility subjected to vertical motions. Earthq Eng Struct Dyn 2013;42:1931–49. doi:10.1002/eqe.2305.
[11] Ryan KL, Soroushian S, Maragakis EM, Sato E, Sasaki T, Okazaki T. Seismic simulation of an integrated ceiling-partition wall-piping system at E-Defense. I: three--dimensional structural response and base isolation. J Struct Eng 2016;142(2) 04015130-1-15.
[12] Soroushian S, Maragakis EM, Ryan KL, Sato E, Sasaki T, Okazaki T, Mosqueda G. Seismic simulation of an integrated ceiling-partition wall-piping system at E-Defense. II: evaluation of nonstructural damage and fragilities. J Struct Eng 2016;142(2) 04015131-1-17.
[13] American Society of Civil Engineers (ASCE). Seismic design requirements for seismically isolated structures. Chapter 17 and commentary in ASCE 7-16: minimum design loads for buildings and other structures. Reston, VA; 2017.
[14] Warn GP, Ryan KL. A review of seismic isolation for buildings: historical development and research needs. Buildings 2012;2(4):300–25. doi:10.3390/buildings2030300.
[15] Malushte S, Whittaker A. Survey of past base isolation applications in nuclear power plants and challenges to industry/regulatory acceptance. In: Proceedings of the 18th International Conference. Beijing, China: SMiRT 18; 2005.
[16] Aiken ID, Kelly JM, Tajirian FF. Mechanics of low shape factor elastomeric seismic isolation bearings. Berkeley, California; 1989.
[17] Kelly JM. Base isolation in Japan. Report No. UCB/EERC-88/20. Berkeley, CA: Earthquake Engineering Research Center, University of California; 1988.
[18] Tajirian FF, Kelly JM, Aiken ID, Veljovich W. Elastomeric bearings for three-dimensional seismic isolation. In: Proceedings of the SME PVP conference. Nashville, Tennessee; 1990.
[19] Huffmann GK. Full base isolation for earthquake protection by helical springs and viscodampers. Nucl Eng Des 1985;84(3):331–8.
[20] Makris N, Deoskar H. Prediction of observed response of base-isolated structure. J Struct Eng 1996;122(5).
[21] Suhara J, Tamura T, Ohta K, Okada Y, Moro S. Research on 3-D base isolation system applied to new power reactor 3-D seismic isolation device with rolling seal type air spring: part 1. In: Proceedings of the 17th international conference on structural mechanics in reactor technology (SMiRT 17); 2003. p. 1–6.
[22] Suhara J, Matsumoto R, Oguri S, Okada Y, Inoue K, Takahashi K. Research on 3-D base isolation system applied to new power reactor 3-D seismic isolation device with rolling seal type air spring: part 2. In: Proceedings of the 18th international conference on structural mechanics in reactor technology (SMiRT 18); 2005. p. 3381–91.
[23] Kageyama M, Iba T, Umeki K, Somaki T, Moro S. Development of three -dimensional base isolation system with cable reinforcing air spring. In: Proceedings of the 17th international conference on structural mechanics in reactor technology (SMiRT 17); 2003. p. 17–22. Division K, paper no. K09-5.
[24] Kageyama M, Iba T, Umeki K, Somaki T, Hino Y, Moro S, Ikutama S. Study on three--dimensional seismic isolation system for next generation nuclear power plant: independent cable reinforced rolling-seal air spring. In: Proceedings of the 13th world conference on earthquake engineering; 2004. p. 1–6. paper no. 1346.
[25] Lee Y, Ji YS, Han W, Choi S, Cho SG. Shaking table test of vertical isolation device. Int J Environ Sci Dev 2014;5(1):5–7.
[26] Tsujiuchi N, Ito A, Sekiya Y. Characterization and performance evaluation of a vertical seismic isolator using link and crank mechanism. J Phys Conf Ser 2016;744(1).
[28] Lu LY, Chen PR, Pong KW. Theory and experiment of an inertia-type vertical isolation system for seismic protection of equipment. J Sound Vib 2016;366:44–61.
[28] Kitayama S, Lee D, Constantinou MC, Kempner L Jr. Probabilistic seismic assessment of seismically isolated electrical transformers considering vertical isolation and vertical ground motion. Eng Struct 2017;152(152):888–900.
[29] Kordonsky W. Elements and devices based on magnetorheological effect. J Intell Mater Syst Struct 1993;4(1):65–9.
[30] Parlak Z, Engin T, Cesmeci S, Sahin I. Dynamic characterisation of a vehicle magnetorheological shock absorber. Int J Veh Des 2012;59(2/3) pp. 129–14.
[31] Hong S-R, Wang G, Hu W, Wereley NM. Liquid spring shock absorber with controllable magnetorheological damping. Proc Inst Mech Eng Part D J Automob Eng 2006;220(8):1019–29.
[32] G. Hitchcock and F. Gordaninejad, "Controllable compressible fluid damper," US7422092 B2, 2008.
[33] Raja P. Design and development of a compressible magneto-rheological damper. Reno: University of Nevada; 2009.
[34] Raja P, Wang X, Gordaninejad F. A high-force controllable mr fluid damper–liquid spring suspension system. Smart Mater Struct Jan. 2014;23(1):15021.
[35] Potnuru MR, Wang X, Mantripragada S, Gordaninejad F. A compressible magneto-rheological fluid damper – liquid spring system. Int J Veh Des 2013;63(2–3):256–74.
[36] McKee M, Wang X, Gordaninejad F. Effects of temperature on performance of a compressible magnetorheological fluid damper-liquid spring suspension system. J Intell Mater Syst Struct 2017:1–11 no. Special Issue Article.
[37] Maus N, Gordaninejad F. A fail-safe, bi-linear liquid spring controllable magnetorheological fluid damper. In: Proceedings of the SPIE smart structures and materials + nondestructive evaluation and health monitoring; 2014.
[38] Nguyen Q-H, Choi S-B. Optimal design of a vehicle magnetorheological damper considering the damping force and dynamic range. Smart Mater Struct 2009;18(1):015013.
[39] Golinelli N, Spaggiari A. Experimental validation of a novel magnetorheological damper with an internal pressure control. J Intell Mater Syst Struct 2017;28(18):2489–99. doi:10.1177/1045389X17689932.
[40] Gavin H, Hoagg J, Dobossy M. Optimal design of mrf dampers. In: Proceedings of the U.S. - Japan workshop on smart structures for improved seismic performance in urban regions; 2001. p. 225–36.
[41] Cesmeci S. A fail-safe, bi-linear liquid spring, controllable magnetorheological fluid damper for a three-dimensional earthquake isolation system. Reno: University of Nevada; 2017.
[42] Eltahawy W, Ryan KL, Cesmeci S, Gordaninejad F. Displacement/velocity-based control of a liquid spring – MR damper for vertical isolation. Struct Control Health Monitor 2019. doi:10.1002/stc.2363.
[43] Eltahawy W, Ryan KL, Cesmeci S, Gordaninejad F. Parameters affecting dynamics of three-dimensional seismic isolation. J Earthq Eng 2018. doi:10.1080/13632469.2018.1537902.
[44] Yang G, Spencer BF, Carlson JD, Sain MK. Large-scale mr fluid dampers: modeling and dynamic performance considerations. Eng Struct 2002;24:309–23.
[45] Kitayama S, Constantinou MC. Fluidic self-centering devices as elements of seismically resistant structures: description, testing, modeling, and model validation. J Struct Eng 2017;143(7):1–10.
[46] Cesmeci S, Engin T. Modeling and testing of a field-controllable magnetorheological fluid damper. Int J Mech Sci 2010;52:1036–46.
[47] Castaldo P, Gino D, Bertagnoli G, Mancini G. Partial safety factor for resistance model uncertainties in 2D non-linear finite element analysis of reinforced concrete structures. Eng Struct 2018. doi:10.1016/j.engstruct.2018.09.041.

[48] Gordaninejad F, Breese DG. Heating of magnetorheological fluid dampers. J Intell Mater Syst Struct 1999;10(8):634–45.
[49] Sahin I, Cesmeci S, Wilson NL, Wereley NM. Sensitivity of magnetorheological damper behavior to perturbations in temperature via Bouc-Wen model. In: Proceedings of 12th international conference on electro-rheological fluids and magneto-rheological suspensions; 2011. p. 665–71.
[50] Cesmeci S, Wilson NL, Wereley NM, Sahin I. Sensitivity of magnetorheological damper behavior to perturbations in temperature. In: Proceedings of ASME conference on smart materials, adaptive structures and intelligent systems, vol. 2; 2010. p. 433–9. Paper no. SMASIS2010-3802.
[51] McKee M, Wang X, Gordaninejad F. Effects of temperature on performance of a compressible magnetorheological fluid damper-liquid spring suspension system. J. Intell. Mater. Syst. Struct. 2017:1–11 no. Special Issue Article.
[52] Gavin H, Hoagg J, Dobossy M. Optimal design for magnetorheological dampers. In: Proceedings of the U.S. - Japan workshop on smart structures for improved seismic performance in urban regions; 2001. p. 225–36. no. August.
[53] Nguyen QH, Han YM, Choi SB, Wereley NM. Geometry optimization of mr valves constrained in a specific volume using the finite element method. Smart Mater Struct 2007;16(6):2242–52.
[54] Nguyen QH, Choi SB, Kim KS. Geometric optimal design of mr damper considering damping force, control energy and time constant. J Phys Conf Ser 2009;149:012076.
[55] Nguyen QH, Choi SB. Optimal design of a vehicle magnetorheological damper considering the damping force and dynamic range. Smart Mater Struct 2009;18(1).
[56] Mangal SK, Kumar A. Geometric parameter optimization of magneto-rheological damper using design of experiment technique. Int J Mech Mater Eng 2015;10(1):1–9.
[57] Zhang X, Li Z, Guo K, Zheng F, Wang Z. A novel pumping magnetorheological damper: design, optimization, and evaluation. J Intell Mater Syst Struct 2017;28(17):2339–48.
[58] Spaggiari A, Dragoni E. Effect of pressure on the physical properties of magnetorheological fluids. Frattura ed Integrità Strutturale Jan. 2013;7(23):75–86.
[59] Spaggiari A, Dragoni E. Combined squeeze-shear properties of magnetorheological fluids: effect of pressure. J Intell Mater Syst Struct 2014;25(9):1041–53.
[60] Becnel AC, Sherman SG, Hu W, Wereley NM. Squeeze strengthening of magnetorheological fluids using mixed mode operation. J Appl Phys 2015;117(17):1–5.
[61] Tang X, Zhang X, Tao R, Rong Y. Structure-enhanced yield stress of magnetorheological fluids. J Appl Phys 2000;87(5):2634–8.
[62] Spaggiari A, Dragoni E. Enhanced properties of magnetorheological fluids: effect of pressure. J Intell Mater Syst Struct 2015;26(14):1764–75.
[63] Zhang XZ, Gong XL, Zhang PQ, Wang QM. Study on the mechanism of the squeeze-strengthen effect in magnetorheological fluids. J Appl Phys 2004;96(4):2359–64.
[64] Wang X, Gordaninejad F. Lyapunov-based control of a bridge using magnetorheological fluid dampers. J Intell Mater Syst Struct 2002;13(7–8):415–19. doi:10.1106/104538902025939.
[65] Yoshida O, Dyke SJ. Response control of full-scale irregular buildings using magnetorheological dampers. J Struct Eng 2005;131(5):734–42. doi:10.1061/(ASCE)0733-9445(2005)131:5(734).
[66] Rahbari NM, Azar BF, Talatahari S, Safari H. Semi-active direct control method for seismic alleviation of structures using MR dampers. Struct Control Health Monit 2013;20:1021–42. doi:10.1002/stc.1515.
[67] Xu Z-D, Zhao Y-L, Guo Y-Q, Yang X-L, Sarwar W. Shaking table tests of magnetorheological damped frame to mitigate the response under real-time online control. Smart Mater Struct 2019;28(11). doi:10.1088/1361-665X/ab45fd.
[68] Eltahawy W, Ryan KL, Cesmeci, Gordaninejad F. Fundamental dynamics of 3-dimensional seismic isolation. Proceedings of the 16th World Conference on Earthquake Engineering. Chile: NICEE; 2017.
[69] Eltahawy W, Ryan KL, Cesmeci S, Gordaninejad F. Control strategy for liquid spring - MR damper for vertical isolation. 11th U.S. National Conference on Earthquake Engineering: Integrating Science, Engineering & Policy. Los Angeles, California: NCEE; 2018.
[70] Parlak Z, Engin T, Calli I. Optimal design of MR damper via finite element analyses of fluid dynamic and magnetic field. Mechatronics 2012;22(6):890–903. doi:10.1016/j.mechatronics.2012.05.007.

Sevki Cesmeci, Ph.D. Dr. Cesmeci currently works as an Assistant Professor of Mechanical Engineering at Georgia Southern University. He received his Ph.D. in Mechanical Engineering from University of Nevada, Reno in 2017. His Ph.D. project was about seismic resillience of large building structures, which was funded by the U.S. National Science Foundation. His current research areas include engineering applications of thermal-fluid sciences, smart materials and structures, and seismic isolation in general, and innovative seal systems for turbomachinery and magnetorheological dampers and their application in particular.

Faramarz Gordaninejad, Ph.D. Dr. Gordaninejad is a Regents and Foundation Professor Emeritus of Mechanical Engineering, University of Nevada, Reno. He has served as the President and CEO of Advanced Materials and Devices, Inc. (www.amadinc.com) for the last 20 years. Dr. Gordaninejad's research focuses on fundamental studies on theoretical and experimental mechanics, fiber-reinforced composite-materials elements and structures, heat transfer, and basic and applied research on MR- based system for vehicles and structural control and safety. He has led research projects from various government agencies, and leading industries, and has more than 300 technical publications. Dr. Gordaninejad is a fellow of American Society of Mechanical Engineers (ASME), Society for Advancement of Material and Process Engineering (SAMPE), and the International Society for Optics and Photonics (SPIE).

Keri L. Ryan, Ph.D. Dr. Ryan is an associate professor in the CEE Department, specializing in the earthquake and structural engineering sub-discipline. The overarching theme of her research is development of engineering concepts and techniques for improved seismic performance, with primary applications in buildings. Much of her work has focused on seismic isolation, and she has been awarded three major National Science Foundation projects focused in this area. She led an international collaborative test program between the U.S. and Japan that conducted shake table testing of a full scale building with and without seismic isolation. This led to groundbreaking discoveries on the effect of vertical shaking, and horizontal-vertical coupling responses in buildings. Recently, Dr. Ryan has diversified her research portfolio, and has recent or ongoing projects in the areas of nonstructural components, and lower damage structural systems for timber and concrete.

Walaa Eltahawy, Ph.D. Dr. Eltahawy is a recent Ph.D. graduate of the Department of Mechanical Engineering and Civil and Environmental Engineering, University of Nevada, Reno. During her Ph.D., Dr. Eltahawy worked as Research Assistant in a National Science Foundation project about 3D seismic isolation of large building structures. Her research areas include structural dynamics, earthquake engineering, and dynamic analysis.